A phase-field model for mixed-mode fracture based on a unified tensile fracture criterion

Qiao Wang[1,2], **Y.T. Feng**[2], **Wei Zhou**[1], **Yonggang Cheng**[1], **Gang Ma**[1]

[1]*State Key Laboratory of Water Resources and Hydropower Engineering Science, Wuhan University, Wuhan 430072, China*

[2] *Zienkiewicz Centre for Computational Engineering, Swansea University, UK*

Abstract

Different fracture patterns can be observed because of different material properties, even the geometry and loading are the same. However, most of the known phase-field fracture models have only considered the tensile failure and may not be directly applicable to the shear fracture. In this paper, a phase-field model for mixed-mode fracture is proposed based on a unified tensile fracture criterion. The proposed model is developed from the unified phase-field theory and the original unified phase-field model can be recovered as a particular case. General softening laws for cohesive zone models can also be considered. The unified tensile fracture criterion is embedded in the proposed mixed-mode phase-field model and different fracture patterns can be obtained in the simulation according to the material properties, including failures based on both maximum normal stress and maximum shear stress criteria. The crack propagation direction can be easily determined by the unified tensile fracture criterion. Compared with the classical phase-field model, two additional material parameters are needed, i.e., the failure tension strength and the ratio of the critical shear failure stress to the critical normal fracture stress. Numerical examples have shown that the proposed model has the ability to model mixed-mode fractures, and can also be applied to rock-like brittle materials under compression.

Keywords: phase-field fracture model; shear fracture; mixed-mode fracture; unified tensile fracture criterion.

1. Introduction

Many numerical methods have been developed for modeling the crack propagation in solids, such as the extended finite element method (XFEM) [1, 2], the meshfree methods [3], the peridynamics [4, 5], the cracking particle method (CPM) [6, 7], the screened Poisson equation [8, 9], the cellular automaton method [10, 11] and the phase-field models [12-15]. The phase-field models have attracted much attention recently. In the phase-field models, a new variable called the phase-field is introduced to represent the damage of the material [16], and the discontinuity and singularity caused by the crack can be avoided in simulations. The phase-field distribution can be obtained by solving a multi-physics problem and the crack propagation can be tracked automatically.

The phase-field models are mainly based on the Landau-Ginzburg phase transition in physics communities [17-22] and Griffith's theory in mechanics communities [16, 23-25]. The phase-field models based on Griffith's theory are derived from the regularized form [16] of the variational formulation [25] from Griffith's theory. There are two functions, *crack surface density function* and *degradation function*, in the phase-field models. The crack surface density function controls the distribution of the phased-field in the domain and the degradation function characterizes the energy transfer between the phase-field and the displacement field. Different crack surface density functions and degradation functions result in different phase-field models. Recently, a unified phase-field theory [26] was proposed and most of the known phase-field models can be recovered as its special cases. Most importantly, general softening laws can be implemented in the unified phase-field theory and the length scale has little influence on the global responses. Another important function in phase-field models is the *energy density function*, which controls the bulk energy of the solid, and some decompositions of the energy density function were proposed to avoid damage in the compressive state [23, 27-31].

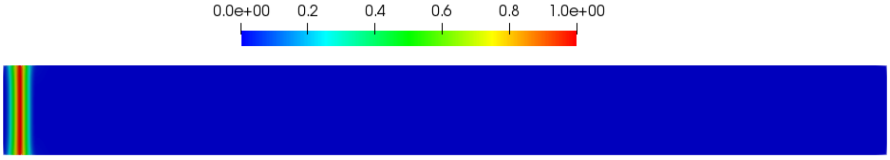

(a) Crack obtained by most phase-field models: $\theta_T = \pi / 2$

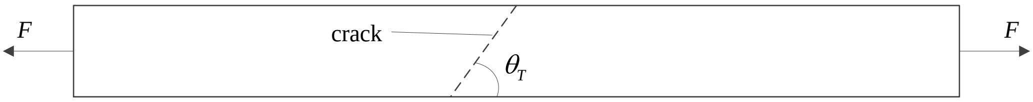

(b) Crack angle observed in physical experiment: $\theta_T \in [\pi / 4, \pi / 2]$

Figure 1. Fracture angle for the long bar under tensional loading

The phase-field models have been applied in many areas, such as dynamic analysis [12, 32-37], fractures in thin shells [38, 39], fracture in heterogeneous structure [40], cohesive fracture [26, 41-46] and brittle-ductile dynamic failure [47]. In the phase-field models, the fracture criterion is embedded implicitly and no additional criterion is needed. In most phase-field models based on Griffith's theory, the G-criterion is embedded and only the fracture energy G_c is used. The fracture energy G_c used in most of these phase-field models is the mode-I fracture energy or fracture energy for a tensile failure. Thus, these phase-field models cannot be applied to shear failure, or mixed-mode fracture mainly based on Mode-II fracture. This G-criterion is more like the maximum tensile strain criterion or maximum normal stress criterion, and only the fracture angle $\theta_T = \pi / 2$ can be obtained for a long bar under tensional loading (see Figure 1(a)). However, the fracture behavior may differ widely for different materials. For example, the fracture angle θ_T is between $\pi / 4$ and $\pi / 2$ for many different metallic glasses in physical experiments (see Figure 1(b)) [48]. Especially, the shear fracture will occur at $\theta_T = \pi/4$ according to the maximum shear stress criterion (Tresca criterion).

To consider the mixed-mode crack propagation in rock-like materials, a modification of the classical phase-field model [49] was proposed by decomposing the history variable into two components, and a modified G-criterion [50] is applied, in which two fracture energies G_I and G_{II} are considered. Another important phase-field model for mixed-mode fracture based on the modified G-criterion and consistent kinematic modes was proposed for anisotropic rocks [51]. In this model, the crack propagation direction and the kinematics modes are determined by a local maximization problem.

In this work, a new mixed-mode phase-field fracture model is proposed by considering the unified tensile fracture criterion [48]. The classical four failure criteria, i.e., maximum normal stress criterion, Tresca criterion, Mohr-Coulomb criterion, and von Mises criterion are special cases of the unified tensile fracture criterion. Thus, the proposed phase-field model can simulate mode-I, mode-II, and mixed mode-I/II fractures according to the material property. The crack propagation direction can be determined easily by the unified tensile fracture criterion. Compared with the classical phase-field model, two additional material parameters, i.e. the failure tension strength and the ratio of the critical shear failure stress to the critical normal fracture stress, are needed. The proposed model is derived in the framework of the unified phase-field theory [26], and general softening laws for cohesive zone models can be implemented [52]. The original unified phase-field model can be recovered as a particular case of the proposed model and an analytical solution for a 2D long bar under tensional loading is provided. Numerical examples have shown that the fracture angle $\theta_T \to \pi / 4$ can be observed for the long bar under tensional loading by the proposed phase-field model according to the Tresca criterion. The proposed model can also be applied for simulating rock-like materials under compression.

This paper is organized as follows. In Section 2, the phase-field model based on the unified phase-field theory is introduced. The mixed-mode phase-field model based on the unified tensile fracture criterion is proposed in Section 3, followed by the analytical solution for a 2D long bar under tensional loading in Section 4. Then the numerical implementation and numerical examples are presented in Sections 5 and 6, respectively.

2. The phase-field model

2.1 The governing equations of the phase-field model

In this section, the phase-field model based on the variational approach of Griffith's theory [16, 53] is introduced. The total energy function without the body force can be written as

$$\mathrm{E}=\int_{\Omega}\psi_0(\boldsymbol{\varepsilon}(\mathbf{u}))\mathrm{d}\Omega+G_c\int_{\Gamma_c}\mathrm{d}\Gamma_c-\int_{\partial\Omega}\bar{\mathbf{t}}\cdot\mathbf{u}\mathrm{d}\partial\Omega \tag{1}$$

where Ω is a bounded domain with boundary $\partial\Omega$, $\Gamma_c\subset\Omega$ is the crack set, $\mathbf{u}$ is the displacement, $\bar{\mathbf{t}}$ is the prescribed surface traction, $\boldsymbol{\varepsilon}$ is the strain tensor, G_c is the material fracture toughness or energy, and ψ_0 is the initial energy density function defined as

$$\psi_0=\frac{1}{2}\lambda\mathrm{tr}^2[\boldsymbol{\varepsilon}]+\mu\mathrm{tr}[\boldsymbol{\varepsilon}^2] \tag{2}$$

where λ and μ are the Lame constants.

The regularized form of Equation (1) can be obtained by introducing a variable s called phase-field as

$$\mathrm{E}(\mathbf{u},s)=\int_{\Omega}\psi(\boldsymbol{\varepsilon}(\mathbf{u}),s)\mathrm{d}\Omega+G_c\int_{\Omega}\gamma(s,\nabla s)\mathrm{d}\Omega-\int_{\partial\Omega}\bar{\mathbf{t}}\cdot\mathbf{u}\mathrm{d}\partial\Omega \tag{3}$$

where $\gamma(s,\nabla s)$ is the surface density function expressed in terms of the crack surface field $s\in[0,1]$, and $\psi(\boldsymbol{\varepsilon}(\mathbf{u}),s)=\omega(s)\psi_0(\boldsymbol{\varepsilon}(\mathbf{u}))$ is the modified energy density function, in which $\omega(s)\in[0,1]$ is the degradation function.

The problem is reduced to finding both phase-field and displacement field on the solid and the variation of Equation (3) can be written as

$$\begin{aligned}\delta\mathrm{E}(\mathbf{u},s)&=\int_{\Omega}\boldsymbol{\sigma}(\mathbf{u},s):\delta\boldsymbol{\varepsilon}\mathrm{d}\Omega+\int_{\Omega}\frac{\partial\psi(\boldsymbol{\varepsilon},s)}{\partial s}\delta s\mathrm{d}\Omega\\&+\int_{\Omega}G_c[\frac{\partial\gamma(s,\nabla s)}{\partial s}\delta s+\frac{\partial\gamma(s,\nabla s)}{\partial\nabla s}\cdot\delta(\nabla s)]\mathrm{d}\Omega-\int_{\partial\Omega}\bar{\mathbf{t}}\cdot\delta\mathbf{u}\mathrm{d}\partial\Omega\end{aligned} \tag{4}$$

where the stress tensor $\boldsymbol{\sigma}(\mathbf{u},s)$ is defined as

$$\boldsymbol{\sigma}(\mathbf{u},s)=\frac{\partial\psi(\boldsymbol{\varepsilon},s)}{\partial\boldsymbol{\varepsilon}} \tag{5}$$

By applying the divergence theorem, Equation (4) will be

$$\begin{aligned}\delta \mathrm{E}(\mathbf{u},s) &= -\int_{\Omega} \operatorname{div}\boldsymbol{\sigma}(\mathbf{u})\cdot\delta\mathbf{u}\mathrm{d}\Omega + \int_{\partial\Omega} \boldsymbol{\sigma}(\mathbf{u})\bar{\mathbf{n}}\cdot\delta\mathbf{u}\mathrm{d}\partial\Omega - \int_{\partial\Omega} \bar{\mathbf{t}}\cdot\delta\mathbf{u}\mathrm{d}\partial\Omega \\ &+\int_{\Omega} [-G_c\nabla\cdot(\frac{\partial\gamma(s,\nabla s)}{\partial\nabla s}) + G_c\frac{\partial\gamma(s,\nabla s)}{\partial s} + \frac{\partial\psi(\boldsymbol{\varepsilon},s)}{\partial s}]\delta s\mathrm{d}\Omega + \int_{\partial\Omega} G_c\frac{\partial\gamma(s,\nabla s)}{\partial\nabla s}\bar{\mathbf{n}}\delta s\mathrm{d}\partial\Omega\end{aligned} \tag{6}$$

where $\bar{\mathbf{n}}$ is the unit outward normal at the boundary $\partial\Omega$. Then the governing equation for the phase-field model can be expressed as

$$\operatorname{div}\boldsymbol{\sigma} = \mathbf{0} \tag{7}$$

$$\begin{cases} G_c\nabla\cdot(\frac{\partial\gamma(s,\nabla s)}{\partial\nabla s}) - G_c\frac{\partial\gamma(s,\nabla s)}{\partial s} - \frac{\partial\psi(\boldsymbol{\varepsilon},s)}{\partial s} = 0, & \delta s > 0 \\ G_c\nabla\cdot(\frac{\partial\gamma(s,\nabla s)}{\partial\nabla s}) - G_c\frac{\partial\gamma(s,\nabla s)}{\partial s} - \frac{\partial\psi(\boldsymbol{\varepsilon},s)}{\partial s} < 0, & \delta s = 0 \end{cases} \tag{8}$$

with boundary conditions

$$\begin{cases} \boldsymbol{\sigma}(\mathbf{u})\bar{\mathbf{n}} = \bar{\mathbf{t}} & \text{on} \quad \partial\Omega_t \\ \mathbf{u} = \bar{\mathbf{u}} & \text{on} \quad \partial\Omega_u \end{cases} \tag{9}$$

$$\frac{\partial\gamma}{\partial\nabla s}\cdot\bar{\mathbf{n}} = 0 \qquad \text{on} \quad \partial\Omega \tag{10}$$

where $\bar{\mathbf{u}}$ is the prescribed displacement, $\partial\Omega = \partial\Omega_u \bigcup \partial\Omega_t$, $\partial\Omega_u$ and $\partial\Omega_t$ are the displacement and traction boundaries, respectively. Equations (7) and (8) can be called the equilibrium equation and the evolution equation, respectively.

2.2 The surface density function and the degradation function

The generic form of the crack surface density function proposed in the unified phase-field theory [26] is considered in this paper and it can be written as

$$\gamma(s,\nabla s) = \frac{1}{c_0}(\frac{1}{l_0}\alpha(s) + l_0|\nabla s|^2) \tag{11}$$

with

$$\alpha(s) = \xi_1 s + \xi_2 s^2 + \cdots + \xi_m s^m, \qquad \sum_{i=1}^{m} \xi_i = 1 \tag{12}$$

$$c_0 = 4\int_0^1 \sqrt{\alpha(x)}\mathrm{d}x \tag{13}$$

where $\alpha(s)$ is the geometric crack function and l_0 is the length scale regularizing the crack. In this paper, the following geometric crack function is applied

$$\alpha(s) = 2s - s^2 \tag{14}$$

and $c_0 = \pi$. In the classical phase-field model, $\alpha(s) = s^2$ and $c_0 = 2$ are applied.

The degradation function $\omega(s)$ has the following properties [54]

$$\omega(0)=1, \qquad \omega(1)=0, \qquad \omega'(1)=0 \tag{15}$$

and in the unified phase-field theory, it is defined as

$$\omega(s)=\frac{(1-s)^p}{(1-s)^p+Q(s)}=\frac{1}{1+\phi(s)}, \qquad \phi(s)=\frac{Q(s)}{(1-s)^p} \tag{16}$$

where $p>0$, $Q(s)\geq 0$ and

$$\begin{aligned} Q(s) &= a_1 s + a_1 a_2 s^2 + a_1 a_2 a_3 s^3 + a_1 a_2 a_3 a_4 s^3 + \cdots \\ &= a_1 s + a_1 b_2 s^2 + a_1 b_3 s^3 + a_1 b_4 s^3 + \cdots \end{aligned} \tag{17}$$

in which $b_i=\prod_{j=2}^{i} a_j$ are coefficients calibrated from material properties or cohesive models, and some details can be found in the unified phase-field theory [26].

Using Equation (11), Equation (8) can be written as

$$\begin{cases} \dfrac{2G_c l_0}{c_0}\nabla^2 s-\dfrac{G_c}{c_0 l_0}\alpha'(s)-\omega'(s)\psi_0=0, & \delta s>0 \\ \dfrac{2G_c l_0}{c_0}\nabla^2 s-\dfrac{G_c}{c_0 l_0}\alpha'(s)-\omega'(s)\psi_0<0, & \delta s=0 \end{cases} \tag{18}$$

3. The mixed-mode phase-field model based on unified tensile fracture criterion

In this section, the phase-field model for mixed-mode fracture is proposed in the 2D case. Equation (18) can be rewritten as

$$\omega'(s)\frac{\psi_0}{G_c}\geq\frac{2l_0}{c_0}\nabla^2 s-\frac{\alpha'(s)}{c_0 l_0} \tag{19}$$

3.1 Phase-field model based on the maximum normal stress criterion

Take the plane stress problem as an example, and assume that the material will fail only when the first principal normal stress exceeds the critical normal fracture stress. The energy density can be decomposed as

$$\psi=\omega_I(s)\psi_{0I}+\psi_{0II} \tag{20}$$

where ω_I is a degradation function defined as $\omega_I=1/[1+\phi_I(s)]$, ψ_{0I} and ψ_{0II} are defined as

$$\psi_{0I}=\frac{1}{2E}(\bar{\sigma}^{\mathbf{nn}})^2+\frac{1}{2E}(\bar{\sigma}^{\mathbf{mm}})^2-\frac{\nu}{E}\bar{\sigma}^{\mathbf{nn}}\bar{\sigma}^{\mathbf{mm}} \tag{21}$$

$$\psi_{0II}=\frac{1}{2\mu}(\bar{\sigma}^{\mathbf{nm}})^2=\frac{\bar{\tau}^2}{2\mu} \tag{22}$$

where E is the elasticity modulus, ν is the Poisson's ratio, The direction $\mathbf{n}$ is perpendicular to the crack surface and the direction $\mathbf{m}$ is parallel to the crack surface. $\bar{\sigma}^{\mathbf{nn}}$, $\bar{\sigma}^{\mathbf{mm}}$ and $\bar{\sigma}^{\mathbf{nm}} = \bar{\tau}$ are components of the effective stress tensor $\bar{\boldsymbol{\sigma}}$ in the local coordinate system LCS ($\mathbf{n}, \mathbf{m}$) constituted by directions $\mathbf{n}$ and $\mathbf{m}$. The effective stress tensor $\bar{\boldsymbol{\sigma}}$ is defined as

$$\bar{\boldsymbol{\sigma}} = \boldsymbol{\Lambda}\boldsymbol{\varepsilon} \tag{23}$$

where $\boldsymbol{\Lambda}$ is the standard elasticity tensor [31].

The effective constitutive matrix in LCS ($\mathbf{n}, \mathbf{m}$) can be computed by

$$\mathbf{D}_I(\mathbf{n}, \mathbf{m}) = \frac{E}{(1-v^2)^2} \begin{bmatrix} \omega_I(s)(1-v^2) & \omega_I(s)(v-v^3) & 0 \\ \omega_I(s)(v-v^3) & \omega_I(s)(1-v^2) & 0 \\ 0 & 0 & \mu \end{bmatrix} \tag{24}$$

The relation between $\bar{\boldsymbol{\sigma}}$ and $\boldsymbol{\sigma}$ can be obtained as

$$\begin{bmatrix} \bar{\sigma}^{\mathbf{nn}} \\ \bar{\sigma}^{\mathbf{mm}} \\ \bar{\sigma}^{\mathbf{nm}} \end{bmatrix} = \begin{bmatrix} \dfrac{1}{\omega_I(s)} & 0 & 0 \\ 0 & \dfrac{1}{\omega_I(s)} & 0 \\ 0 & 0 & 1 \end{bmatrix} \begin{bmatrix} \sigma^{\mathbf{nn}} \\ \sigma^{\mathbf{mm}} \\ \sigma^{\mathbf{nm}} \end{bmatrix} \tag{25}$$

Then Equation (21) can be written as

$$\psi_{0I} = [\frac{1}{2E}(\sigma^{\mathbf{nn}})^2 + \frac{1}{2E}(\sigma^{\mathbf{mm}})^2 - \frac{v}{E}\sigma^{\mathbf{nn}}\sigma^{\mathbf{mm}}][1+\phi_I(s)]^2 \tag{26}$$

Consider a sufficiently long 2D bar loaded at both ends by a uniform tension (see Figure 2), and assume $\mathbf{n}$ is the direction of the first major principle stress of the stress tensor, i.e., $\sigma^{\mathbf{nn}} = \sigma_1$, $\sigma^{\mathbf{mm}} = \sigma_2 = 0$, where σ_1 and σ_2 are the first and second major principle stresses, respectively. Then for the case $\delta s > 0$, Equation (19) can be rewritten as

$$2l_0^2\nabla^2 s - \alpha'(s) + \frac{c_0 l_0}{2E}\frac{\sigma_1^2}{G_{cI}}\phi_I'(s) = 0 \tag{27}$$

or, equivalently,

$$(l_0\nabla s)^2 - \alpha(s) + \frac{c_0 l_0}{2E}\frac{\sigma_1^2}{G_{cI}}\phi_I(s) = 0 \tag{28}$$

where G_{cI} is the fracture energy for the Mode-I fracture.

The crack initiation is assumed at the middle point, then the stress σ_1 at the middle point can be computed by

$$\sigma_1(s^*) = \sqrt{\frac{2EG_{cI}}{c_0 l_0}\frac{\alpha(s^*)}{\phi_I(s^*)}} \tag{29}$$

where s^* is the maximum phase-field and the condition $\nabla s = 0$ at the middle point is applied.

In the unified phase-field model, the critical normal tensile fracture stress σ_t can be evaluated by setting $s^* \to 0$ and

$$\sigma_t = \lim_{s^* \to 0} \sigma_1(s^*) = \sqrt{\frac{2EG_{cI}}{c_0 l_0} \frac{\alpha'(0)}{\phi_I'(0)}} \tag{30}$$

where the L'Hoptial's rule is applied because $\alpha(0) = \phi_I(0) = 0$, and the Mode-I fracture energy can be computed by

$$G_{cI} = \frac{c_0 l_0}{2E} \frac{\phi_I'(0)}{\alpha'(0)} \sigma_t^2 \tag{31}$$

Substituting Equations (21) and (31) into Equation (19), one can obtain

$$\frac{\bar{\sigma}_1^2}{\sigma_t^2} \le [\frac{2l_0^2}{\omega_I'(s)} \nabla^2 s - \frac{\alpha'(s)}{\omega_I'(s)}] \frac{\phi_I'(0)}{\alpha'(0)} \tag{32}$$

or

$$\frac{\sigma_1^2}{\sigma_t^2} \le -\frac{2l_0^2 \nabla^2 s - \alpha'(s)}{\alpha'(0)} \frac{\phi_I'(0)}{\phi_I'(s)} \tag{33}$$

where $\bar{\sigma}_1$ is the first major principle value of the effective stress tensor $\bar{\boldsymbol{\sigma}}$. It can be indicated that Equation (32) or (33) is similar to the maximum normal stress criterion.

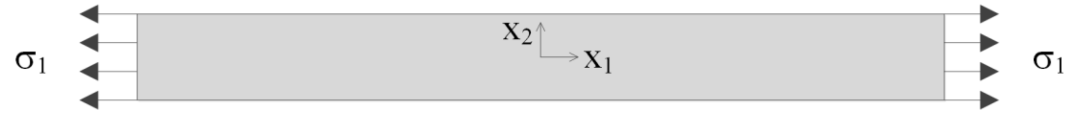

Figure 2. The long bar under tensile loading

3.2 Phase-field model based on the maximum shear stress criterion

Similarly, one can assume that the material will fail only when the shear stress exceeds the critical shear fracture stress. The energy density can be decomposed as

$$\psi = \omega_{II}(s)\psi_{0II} + \psi_{0I} \tag{34}$$

where ψ_{0I} and ψ_{0II} are defined in Equations (21) and (22), respectively, and $\omega_{II} = 1/[1+\phi_{II}(s)]$.

In this case, the effective constitutive matrix in LCS ($\mathbf{n},\mathbf{m}$) can be computed by

$$\mathbf{D}_{II}(\mathbf{n},\mathbf{m}) = \frac{E}{(1-v^2)^2} \begin{bmatrix} 1-v^2 & v-v^3 & 0 \\ v-v^3 & 1-v^2 & 0 \\ 0 & 0 & \omega_{II}(s)\mu \end{bmatrix} \tag{35}$$

and one can obtain

$$\bar{\sigma}^{\mathbf{nm}} = \bar{\tau} = [1+\phi_{II}(s)]\sigma^{\mathbf{nm}} = [1+\phi_{II}(s)]\tau \tag{36}$$

where $\bar{\tau} = \bar{\sigma}^{\mathbf{nm}}$ and $\tau = \sigma^{\mathbf{nm}}$.

Then ψ_{0II} in Equation (22) can be computed as

$$\psi_{0II} = \frac{\bar{\tau}^2}{2\mu} = [1+\phi_{II}(s)]^2 \frac{\tau^2}{2\mu} \tag{37}$$

Substituting Equation (37) into Equation (19) for the case $\delta s > 0$ leads to

$$2l_0^2\nabla^2 s - \alpha'(s) + \frac{c_0 l_0}{2\mu}\frac{\tau^2}{G_{cII}}\phi'_{II}(s) = 0 \tag{38}$$

where ψ_0 and G_c are replaced by ψ_{0II} and G_{cII}, respectively.

Similarly, consider a long bar with loading shown in Figure 2, and assume that $\mathbf{m}$ is the direction of the maximum shear stress. Also assume that the crack initiates at the middle point, then the maximum shear stress can be computed by

$$\tau(s^*) = \sqrt{\frac{2\mu G_{cII}}{c_0 l_0}\frac{\alpha(s^*)}{\phi_{II}(s^*)}} \tag{39}$$

and the critical shear failure stress τ_s is

$$\tau_s = \sqrt{\frac{2\mu G_{cII}}{c_0 l_0}\frac{\alpha'(0)}{\phi'_{II}(0)}} \tag{40}$$

where G_{cII} can be computed by

$$G_{cII} = \frac{c_0 l_0}{2\mu}\frac{\phi'_{II}(0)}{\alpha'(0)}\tau_s^2 = \frac{\phi'_{II}(0)}{\phi'_I(0)}\frac{G_{cI}E\tau_s^2}{\mu\sigma_t^2} = \chi^2\frac{\phi'_{II}(0)}{\phi'_I(0)}\frac{G_{cI}E}{\mu} \tag{41}$$

in which $\chi = \tau_s / \sigma_t$ can be considered as a material parameter.

Finally, for a model-II fracture, Equation (19) can be rewritten as

$$\frac{\bar{\tau}^2}{\tau_s^2} \le [\frac{2l_0^2}{\omega'_{II}(s)}\nabla^2 s - \frac{\alpha'(s)}{\omega'_{II}(s)}]\frac{\phi'_{II}(0)}{\alpha'(0)} \tag{42}$$

or

$$\frac{\tau^2}{\tau_s^2} \le -\frac{2l_0^2\nabla^2 s - \alpha'(s)}{\alpha'(0)}\frac{\phi'_{II}(0)}{\phi'_{II}(s)} \tag{43}$$

One can find out that Equation (42) or (43) is similar to the Tresca criterion.

3.3 Phase-field model based on the unified failure criterion

To obtain the mixed-mode phase-field model, the energy density can be decomposed as

$$\psi_0 = \omega_I(s)\psi_{0I} + \omega_{II}(s)\psi_{0II} \tag{44}$$

where ψ_{0I} and ψ_{0II} are defined in Equations (21) and (22), respectively, and $\omega_I = 1/[1+\phi_I(s)]$, $\omega_{II} = 1/[1+\phi_{II}(s)]$.

Then the effective constitutive matrix in LCS ($\mathbf{n},\mathbf{m}$) can be computed by

$$\bar{\mathbf{D}}(\mathbf{n},\mathbf{m}) = \frac{E}{(1-v^2)^2}\begin{bmatrix} \omega_I(s)(1-v^2) & \omega_I(s)(v-v^3) & 0 \\ \omega_I(s)(v-v^3) & \omega_I(s)(1-v^2) & 0 \\ 0 & 0 & \omega_{II}(s)\mu \end{bmatrix} \tag{45}$$

and the relation between $\bar{\boldsymbol{\sigma}}$ and $\boldsymbol{\sigma}$ can be obtained as

$$\begin{bmatrix} \bar{\sigma}^{\mathbf{nn}} \\ \bar{\sigma}^{\mathbf{mm}} \\ \bar{\sigma}^{\mathbf{nm}} \end{bmatrix} = \begin{bmatrix} \frac{1}{\omega_I(s)} & 0 & 0 \\ 0 & \frac{1}{\omega_I(s)} & 0 \\ 0 & 0 & \frac{1}{\omega_{II}(s)} \end{bmatrix} \begin{bmatrix} \sigma^{\mathbf{nn}} \\ \sigma^{\mathbf{mm}} \\ \sigma^{\mathbf{nm}} \end{bmatrix} \tag{46}$$

The decomposition in Equation (44) cannot avoid the crack propagation under compressive stress, thus, a modified decomposition can be defined as

$$\psi_0 = \omega_I(s)\psi_{0I}^{+} + \omega_{II}(s)\psi_{0II}^{+} + \psi_0^{-} \tag{47}$$

where

$$\psi_{0I}^{+} = \begin{cases} \frac{(\bar{\sigma}^{\mathbf{nn}})^2}{2E}, & if \quad \bar{\sigma}^{\mathbf{nn}} > 0 \\ 0, & if \quad \bar{\sigma}^{\mathbf{nn}} \le 0 \end{cases} \tag{48}$$

$$\psi_{0II}^{+} = \begin{cases} \frac{(\bar{\sigma}^{\mathbf{nm}})^2}{2\mu} = \frac{\bar{\tau}^2}{2\mu}, & if \quad \bar{\sigma}_1 > 0 \\ 0, & if \quad \bar{\sigma}_1 \le 0 \end{cases} \tag{49}$$

$$\psi_0^{-} = \psi_0 - \psi_{0I}^{+} - \psi_{0II}^{+} \tag{50}$$

In Equation (48), it is assumed $\bar{\sigma}^{\mathbf{nn}} \ge \bar{\sigma}^{\mathbf{mm}}$, and in Equation (49), $\bar{\sigma}_1$ is the first major principle value of the effective stress tensor $\bar{\boldsymbol{\sigma}}$.

Now Equation (19) can be rewritten as

$$\omega_I'(s)\frac{\psi_{0I}^{+}}{G_{cI}} + \omega_{II}'(s)\frac{\psi_{0II}^{+}}{G_{cII}} \ge \frac{2l_0^2\nabla^2 s - \alpha'(s)}{c_0 l_0} \tag{51}$$

By substituting Equations (48), (49), (31), and (41) into Equation (51), and only considering the tensional-shear state, one can have

$$\frac{\bar{\sigma}^2}{\sigma_t^2}\frac{\omega_I'(s)}{\phi_I'(0)}+\frac{\bar{\tau}^2}{\tau_s^2}\frac{\omega_{II}'(s)}{\phi_{II}'(0)}\geq\frac{2l_0^2\nabla^2 s-\alpha'(s)}{\alpha'(0)} \tag{52}$$

where $\bar{\sigma}=\bar{\sigma}^{\mathbf{nn}}$, and $\bar{\tau}=\bar{\sigma}^{\mathbf{nm}}$.

If $\omega_I(s)=\omega_{II}(s)$, Equation (52) will be similar to the unified failure criterion [48], or called as the "ellipse criterion", expressed as

$$\frac{\bar{\sigma}^2}{\sigma_t^2}+\frac{\bar{\tau}^2}{\tau_s^2}=1 \tag{53}$$

For a tensile fracture, the well-known four criteria are special cases of this unified failure criterion:

(i) the Tresca criterion: $\chi=\tau_s/\sigma_t=0$;

(ii) the maximum normal stress criterion: $\chi=\tau_s/\sigma_t>\sqrt{2}/2$;

(iii) the Mohr-Coulomb criterion: $\chi=\tau_s/\sigma_t<\sqrt{2}/2$;

(iv) the von Mises criterion: $\chi=\tau_s/\sigma_t=\sqrt{3}/3$.

There are also some other generic failure criteria for fracture. For example, a more generic failure criterion of either elliptic, parabolic, or hyperbolic type has been analyzed in a unified manner [55-57].

In this paper, the crack propagation direction will be determined based on the unified failure criterion, i.e., Equation (53).

3.4 The crack direction

To determine the direction of the crack based on the unified criterion, one can define a function

$$f(2\theta)=\frac{\bar{\sigma}^2}{\sigma_t^2}+\frac{\bar{\tau}^2}{\tau_s^2}=\frac{(r\cos 2\theta+a)^2}{\sigma_t^2}+\frac{(r\sin 2\theta)^2}{\tau_s^2} \tag{54}$$

where $r=(\bar{\sigma}_1-\bar{\sigma}_2)/2$, $a=(\bar{\sigma}_1+\bar{\sigma}_2)/2$, and θ is the angle between $\bar{\sigma}$ and the effective first major principle stress $\bar{\sigma}_1$ (see Figure 3). Suppose that the fracture occurs at the stress state $[\bar{\sigma},\bar{\tau}]$, then the fracture direction is perpendicular to the direction of stress $\bar{\sigma}$, and the fracture angle is $\theta_T=\pi/2-\theta$.

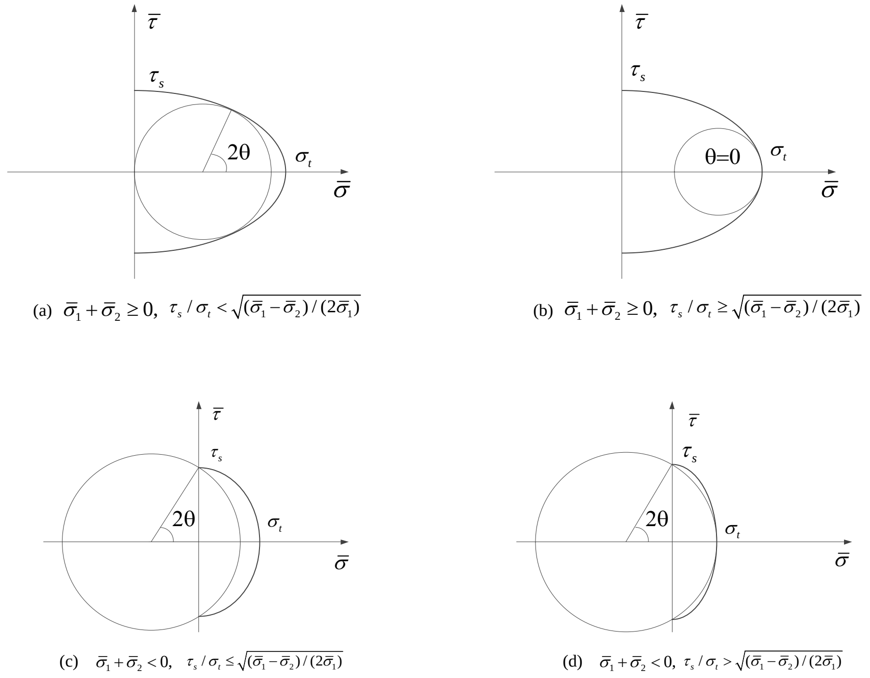

(a) $\bar{\sigma}_1+\bar{\sigma}_2\geq 0,\ \ \tau_s/\sigma_t<\sqrt{(\bar{\sigma}_1-\bar{\sigma}_2)/(2\bar{\sigma}_1)}$

(b) $\bar{\sigma}_1+\bar{\sigma}_2\geq 0,\ \ \tau_s/\sigma_t\geq\sqrt{(\bar{\sigma}_1-\bar{\sigma}_2)/(2\bar{\sigma}_1)}$

(c) $\bar{\sigma}_1+\bar{\sigma}_2<0,\ \ \tau_s/\sigma_t\leq\sqrt{(\bar{\sigma}_1-\bar{\sigma}_2)/(2\bar{\sigma}_1)}$

(d) $\bar{\sigma}_1+\bar{\sigma}_2<0,\ \ \tau_s/\sigma_t>\sqrt{(\bar{\sigma}_1-\bar{\sigma}_2)/(2\bar{\sigma}_1)}$

Figure 3. The crack propagation direction based on unified failure criterion

In the unified failure criterion, the fracture will occur if the function $f(2\theta)\geq 1$ and the value of θ can be computed by

$$\theta=\underset{\theta\in[0,\pi/4]}{\arg\max}\ f(2\theta) \tag{55}$$

To obtain the value of θ, one can define a function f' as

$$f'=\frac{\mathrm{d}f(2\theta)}{\mathrm{d}(2\theta)}=\sin 2\theta\frac{1}{\sigma_t^2}[2r^2(\frac{1-\chi^2}{\chi^2})\cos 2\theta-2ra] \tag{56}$$

Then one can obtain θ for different cases as:

(i) $\bar{\sigma}_1+\bar{\sigma}_2\geq 0$ and $\chi^2\leq(\bar{\sigma}_1-\bar{\sigma}_2)/(2\bar{\sigma}_1)$ (see Figure 3(a))

In this case, $f'>0$ if $\cos 2\theta>\frac{a}{r}\frac{\chi^2}{(1-\chi^2)}$ and $f'<0$ if $\cos 2\theta<\frac{a}{r}\frac{\chi^2}{(1-\chi^2)}$, thus,

$$\theta=\frac{1}{2}\arccos\frac{\bar{\sigma}_1+\bar{\sigma}_2}{\bar{\sigma}_1-\bar{\sigma}_2}\frac{\chi^2}{(1-\chi^2)} \tag{57}$$

(ii) $\bar{\sigma}_1+\bar{\sigma}_2\geq 0$ and $(\bar{\sigma}_1-\bar{\sigma}_2)/(2\bar{\sigma}_1)<\chi^2$ (see Figure 3(b));

In this case, $f'<0$, thus $\theta=0$.

(iii) $\bar{\sigma}_1+\bar{\sigma}_2<0$ and $\chi^2<(\bar{\sigma}_1-\bar{\sigma}_2)/(2\bar{\sigma}_1)$ (see Figure 3(c));

In this case, $f'>0$, thus

$$\theta = \frac{1}{2}\arccos\left|\frac{\bar{\sigma}_1 + \bar{\sigma}_2}{\bar{\sigma}_1 - \bar{\sigma}_2}\right| \tag{58}$$

(iv) $\bar{\sigma}_1 + \bar{\sigma}_2 < 0$ and $\chi^2 \geq (\bar{\sigma}_1 - \bar{\sigma}_2)/(2\bar{\sigma}_1)$ (see Figure 3(d));

In this case, $f' > 0$ if $\cos 2\theta < \frac{a}{r}\frac{\chi^2}{(1-\chi^2)}$ and $f' < 0$ if $\cos 2\theta > \frac{a}{r}\frac{\chi^2}{(1-\chi^2)}$, thus,

$$\theta = 0 \qquad or \quad \theta = \frac{1}{2}\arccos\left|\frac{\bar{\sigma}_1 + \bar{\sigma}_2}{\bar{\sigma}_1 - \bar{\sigma}_2}\right| \tag{59}$$

(v) $\bar{\sigma}_1 < 0$;

In this case, the material is under compressive stress and no damage will be considered, i.e., $\psi_{0I}^{+} = 0$ and $\psi_{0II}^{+} = 0$.

One should note that we can redefine the values of θ and ψ_{0II}^{+} for the case $\bar{\sigma}_1 < 0$ to consider the compressive-shear fracture, which allows the proposed method to model rock-like brittle materials under compression, and the numerical examples are shown in Section 6.4.

3.5 The history fields

In the original unified phase-field model, if the geometric crack function in Equation (14) is used, the distribution of the phase-field is in a finite bounded domain and the boundedness condition of the phase-field cannot be ensured automatically. In this paper, we introduce two *history fields* to overcome this problem.

Equation (28) always holds if $s > 0$ and it also holds when $s = s^* \to 0$, thus, we can have the following equation for Equation (51)

$$\omega_I'(s)\frac{\psi_{0I}^{+}}{G_{cI}} + \omega_{II}'(s)\frac{\psi_{0II}^{+}}{G_{cII}} = \frac{2l_0^2\nabla^2 s - \alpha'(s)}{c_0 l_0} \tag{60}$$

Equation (60) holds for $s > 0$ and $s = s^* \to 0$. The functions $\phi_I(s)$ and $\phi_{II}(s)$ can be defined as

$$\phi_I(s) = b_I\phi(s), \qquad \phi_{II}(s) = b_{II}\phi(s) \tag{61}$$

where b_I and b_{II} are coefficients needed to be determined. Then Equation (60) can be rewritten as

$$\frac{\psi_{0I}^{+}}{\bar{G}_{cI}} + \frac{\psi_{0II}^{+}}{\bar{G}_{cII}} = \frac{\alpha'(0)}{c_0 l_0 \phi'(0)} = \hbar_{\min} \tag{62}$$

when $s = s^* \to 0$, and

$$\bar{G}_{cI} = G_{cI} / b_I = \frac{c_0 l_0}{2E} \frac{\phi'(0)}{\alpha'(0)} \sigma_t^2 \tag{63}$$

$$\bar{G}_{cII} = G_{cII} / b_{II} = \frac{\chi^2 E}{\mu} \bar{G}_{cI} \tag{64}$$

Then one can define two history fields $\hbar_I$ and $\hbar_{II}$ at step m as

$$\begin{cases} \hbar_I(m) = \dfrac{\psi^+_{0I}(m)}{\bar{G}_{cI}}, \hbar_{II} = \dfrac{\psi^+_{0II}(m)}{\bar{G}_{cII}}, & if \quad \dfrac{\psi^+_{0I}(m)}{\bar{G}_{cI}} + \dfrac{\psi^+_{0II}(m)}{\bar{G}_{cII}} > \hbar_I(m-1) + \hbar_{II}(m-1) \\ \hbar_I(m) = \hbar_I(m-1), \hbar_{II} = \hbar_{II}(m-1), & if \quad \dfrac{\psi^+_{0I}(m)}{\bar{G}_{cI}} + \dfrac{\psi^+_{0II}(m)}{\bar{G}_{cII}} \le \hbar_I(m-1) + \hbar_{II}(m-1) \end{cases} \tag{65}$$

where $\hbar_I(0) + \hbar_{II}(0) = \max[\hbar_{\min}, \frac{\psi^+_{0I}(0)}{\bar{G}_{cI}} + \frac{\psi^+_{0II}(0)}{\bar{G}_{cII}}]$ for the initial step 0. With Equation (65), the irreversibility for the crack phase-field evolution can be handled [27].

Finally, the evolution Equation (51) can be rewritten as

$$\frac{\omega_I'(s)}{b_I} \hbar_I + \frac{\omega_{II}'(s)}{b_{II}} \hbar_{II} = \frac{2 l_0^2 \nabla^2 s - \alpha'(s)}{c_0 l_0} \tag{66}$$

For the case $\theta = 0$, it has $\hbar_{II} = 0$ and Equation (66) becomes the evolution equation in the original unified phase-field theory.

4. Analytical solution for the 2D long bar under tension

The analytical solution for the 1D problem under tension has been proposed in [26] and the parameters in Equation (17) are obtained according to a given softening curve. In this section, we will extend the solution to the 2D case for mixed-mode fracture by considering Equation (51).

Considering a 2D long bar with boundary conditions shown in Figure 2, and $\chi = \tau_s / \sigma_t < \sqrt{(\sigma_1 - \sigma_2) / (2\sigma_1)}$ is assumed, where σ_1 and $\sigma_2 = 0$ are the first and second major principal stress.

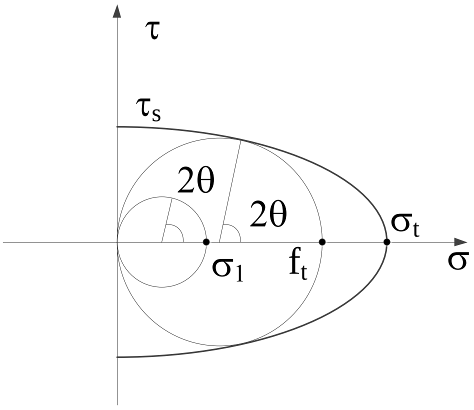

Figure 4. Stress state under tensile loading

According to Equation (57), it has

$$\cos 2\theta = \frac{\chi^2}{1-\chi^2} \tag{67}$$

which means that the angle θ is constant during the loading procedure (see Figure 4). For the case $s > 0$, one can write Equation (52) as

$$\frac{1}{4}\frac{(\sigma_1 \cos 2\theta + \sigma_1)^2}{\sigma_t^2} + \frac{1}{4}\frac{\sigma_1^2 \sin^2 2\theta}{\tau_s^2} = -\frac{2l_0^2\nabla^2 s - \alpha'(s)}{\alpha'(0)}\frac{\phi'(0)}{\phi'(s)} \tag{68}$$

Equation (68) can be simplified to

$$\frac{\sigma_1^2}{\sigma_t^2}\frac{1}{k_1^2} = \frac{2l_0^2\nabla^2 s - \alpha'(s)}{\alpha'(0)}\frac{\phi'(0)}{\phi'(s)} \tag{69}$$

where $k_1 = 2\gamma\sqrt{1-\gamma^2}$.

Substituting Equation (30) into Equation (69) leads to the following equation

$$2l_0^2\nabla^2 s - \alpha'(s) + \frac{\sigma_1^2}{2EG_{cI}}\frac{b_I c_0 l_0}{k_1^2}\phi'(s) = 0 \tag{70}$$

or, equivalently,

$$(l_0\nabla s)^2 - \alpha(s) + \frac{\sigma_1^2}{2EG_{cI}}\frac{b_I c_0 l_0}{k_1^2}\phi(s) = 0 \tag{71}$$

Since $\nabla s = 0$ holds at the middle point, the stress can be computed at this point by

$$\sigma_1(s^*) = \sqrt{\frac{2k_1^2 EG_{cI}}{b_I c_0 l_0}\frac{\alpha(s^*)}{\phi(s^*)}} \tag{72}$$

where s^* is the maximum value of s. The failure tension strength f_t (see Figure 4) can be determined upon the instant of damage initiation, and

$$
\begin{aligned}
f_t &= \lim_{s^* \to 0} \sigma_1(s^*) = \sqrt{\frac{2k_1^2 E G_{cI}}{b_I c_0 l_0} \frac{\alpha(0)}{\phi(0)}} = \sqrt{\frac{2k_1^2 E \bar{G}_{cI}}{c_0 l_0} \frac{\alpha'(0)}{\phi'(0)}} \\
&= k_1 \sigma_t
\end{aligned}
\tag{73}
$$

It can be seen that Equation (71) will be similar to the corresponding equation obtained in [26] if letting

$$
G_c^t = \bar{G}_{cI} k_1^2 \tag{74}
$$

where G_c^t can be considered as the fracture energy obtained from the tensile loading test. Once G_c^t is obtained, the fracture energy $\bar{G}_{cI}$ and $\bar{G}_{cII}$ can be computed by Equations (74) and (64).

Thus, most of the results obtained in [26] can be used in the proposed model directly, such as the parameters for different softening laws. For example, a_1 in Equation (17) can be computed from Equation (73) by

$$
a_1 = \frac{k_1^2}{b_I} \frac{4}{c_0 l_0} \frac{E G_{cI}}{f_t^2} = \frac{4}{c_0 l_0} \frac{E G_c^t}{f_t^2} \tag{75}
$$

which is similar as in [26], and E should be replaced by $E/(1-\nu^2)$ for plane strain problems. For general cases, k_1 is defined as

$$
k_1 = \begin{cases} 2\gamma\sqrt{1-\gamma^2}, & if \quad \gamma < \sqrt{1/2} \\ 1 & otherwise \end{cases} \tag{76}
$$

The other parameters in Equation (17) can be obtained by [26]:

$$
a_2 = \frac{1}{\xi}[(-\frac{4\pi\xi^2}{c_0} \frac{G_c^t}{f_t^2} k_0)^{\frac{2}{3}} + 1] - (p-1) \tag{77}
$$

$$
b_3 + b_4 + \cdots = \begin{cases} 0, & p > 2 \\ \frac{1}{\xi}(\frac{c_0 w_c f_t}{2\pi G_c^t})^2 - (1+a_2), & p = 2 \end{cases} \tag{78}
$$

where k_0 and w_c are the initial slope and the ultimate crake opening, respectively, which can be obtained from given softening laws. In the linear softening law, the other parameters are

$$
a_2 = -\frac{1}{2}, \quad a_i = 0, \quad i \geq 3 \tag{79}
$$

Note that the parameters k_1, $\bar{G}_{cI}$ and $\bar{G}_{cII}$ are independent of the softening law, thus, other geometric crack functions and degradation functions can also be applied in the proposed model, such as the geometric crack function $\alpha(s) = s^2$ and the degradation function $\omega(s) = (1-s)^2$ in the classical model.

5. Numerical implementation

5.1 Calculation parameters

The proposed method can be easily incorporated into the finite element method (FEM). Compared with the classical phase-field model, besides the elasticity modulus E, the Poisson's ratio ν, the fracture energy G_c^t, two additional parameters are needed, i.e., the failure tension strength f_t and the ratio $\chi = \tau_s / \sigma_t$ (see Figure 4). Based on these parameters, the parameter k_1 can be computed by Equation (76), and σ_t, τ_s can be obtained by

$$\sigma_t = f_t / k_1, \qquad \tau_s = \chi \sigma_t \tag{80}$$

The fracture energy G_c^t can be measured from the tension test, then $\bar{G}_{cI}$ and $\bar{G}_{cII}$ can be obtained by $\bar{G}_{cI} = G_c^t / k_1^2$ and $\bar{G}_{cII} = \chi^2 E \bar{G}_{cI} / \mu$. Note that both $\bar{G}_{cI}$ and $\bar{G}_{cII}$ are independent of the parameters b_I and b_{II}.

The parameters b_I and b_{II} will influence the fracture angle in the mixed-mode fracture. From the derivation in Section 3, one can observe that if $b_I = b_{II} = 1$, the proposed model will be simplified and the resulting model can be called a hybrid model, in which the effective constitutive matrix (45) can be written as

$$\bar{\mathbf{D}} = \omega(s)\mathbf{D} \tag{81}$$

where $\mathbf{D}$ is the original constitutive matrix. This hybrid model is similar to the hybrid formulation proposed in [58]. However, this model cannot obtain the correct fracture angle $\pi/4$ for the long bar under tensional loading if the maximum shear stress criterion is applied (i.e., $\chi \to 0$). Thus, the following b_I and b_{II} can be used:

$$b_I = (\cos 2\theta)^n, b_{II} = (\sin 2\theta)^n \tag{82}$$

where θ is the angle obtained in Section 3.5. Our simulations show that b_I and b_{II} may have influence on the fracture angles for some examples. An analytical solution for b_I / b_{II} may exist but is not easy to be obtained.

Similarly, the coefficients b_I and b_{II} at step m can be defined by

$$\begin{cases} b_I(m) = (\cos 2\theta)^n, b_{II} = (\sin 2\theta)^n, & if \quad \dfrac{\psi_{0I}^+(m)}{\bar{G}_{cI}} + \dfrac{\psi_{0II}^+(m)}{\bar{G}_{cII}} > \hbar_I(m-1) + \hbar_{II}(m-1) \\ b_I(m) = b_I(m-1), b_{II} = b_{II}(m-1), & if \quad \dfrac{\psi_{0I}^+(m)}{\bar{G}_{cI}} + \dfrac{\psi_{0II}^+(m)}{\bar{G}_{cII}} \le \hbar_I(m-1) + \hbar_{II}(m-1) \end{cases} \tag{83}$$

5.2 FEM formulations

In the final model proposed for mixed-mode fracture problems, one needs to solve two sub-problems controlled by Equations (7) and (66), respectively. Using FEM, the weak form for Equations (7) and (66) can be written as

$$\int_{\Omega} \mathbf{B}_u^{\mathrm{T}} \hat{\mathbf{D}} \mathbf{B}_u \mathrm{d}\Omega \hat{\mathbf{u}} = \int_{\partial\Omega} \mathbf{\Phi}_u^{\mathrm{T}} \bar{\mathbf{t}} \mathrm{d}\partial\Omega \tag{84}$$

$$\int_{\Omega} \frac{2l_0}{c_0} \mathbf{B}_s^{\mathrm{T}} \mathbf{B}_s \mathrm{d}\Omega \hat{\mathbf{s}} + \int_{\Omega} \frac{1}{c_0 l_0} \alpha'(s) \mathbf{\Phi}_s^{\mathrm{T}} \mathrm{d}\Omega + \int_{\Omega} [\frac{\omega_I'(s)}{b_I} \hbar_I + \frac{\omega_{II}'(s)}{b_{II}} \hbar_{II}] \mathbf{\Phi}_s^{\mathrm{T}} \mathrm{d}\Omega = 0 \tag{85}$$

where $\hat{\mathbf{u}}$ and $\hat{\mathbf{s}}$ are the nodal displacement and nodal phase-field, $\hat{\mathbf{D}}$ is the effective constitutive matrix in the global coordinate system (GCS), and

$$\mathbf{\Phi}_u(\mathbf{x}) = \begin{bmatrix} \Phi^1 & 0 & \Phi^2 & 0 & \cdots & \Phi^N & 0 \\ 0 & \Phi^1 & 0 & \Phi^2 & \cdots & 0 & \Phi^N \end{bmatrix} \tag{86}$$

$$\mathbf{B}_u(\mathbf{x}) = \begin{bmatrix} \Phi^1_{,1} & 0 & \Phi^2_{,1} & 0 & \cdots & \Phi^N_{,1} & 0 \\ 0 & \Phi^1_{,2} & 0 & \Phi^2_{,2} & \cdots & 0 & \Phi^N_{,2} \\ \Phi^1_{,2} & \Phi^1_{,1} & \Phi^2_{,2} & \Phi^2_{,1} & \cdots & \Phi^N_{,2} & \Phi^N_{,1} \end{bmatrix} \tag{87}$$

$$\mathbf{\Phi}_s(\mathbf{x}) = \begin{bmatrix} \Phi^1 & \Phi^2 & \cdots & \Phi^N \end{bmatrix} \tag{88}$$

$$\mathbf{B}_s(\mathbf{x}) = \begin{bmatrix} \Phi^1_{,1} & \Phi^2_{,1} & \cdots & \Phi^N_{,1} \\ \Phi^1_{,2} & \Phi^2_{,2} & \cdots & \Phi^N_{,2} \end{bmatrix} \tag{89}$$

where $\Phi^j = \Phi^j(\mathbf{x})$ is the shape function and N is the total number of discrete nodes.

The whole loading procedure is discretized into M loading steps. In each loading step, Equations (84) and (85) can be solved by monolithic or staggered schemes [24, 27, 54]. In this paper, the staggered scheme is employed, i.e., in each step, the displacement field is solved by Equation (84) with the fixed phase-field, and then the phase-field is solved by Equation (85) with the fixed displacement field. Iterations between these two equations can be performed until the prescribed criterion is reached, which is also known as the alternate minimization algorithm [16].

Equation (84) will result in a non-linear system of equations, which can be solved by direct iteration methods, and in each iteration step, $\hat{\mathbf{D}}$ in GCS can be computed by

$$\hat{\mathbf{D}}^i = [\mathbf{M}(\tilde{\mathbf{n}}^i)]^{\mathrm{T}} \bar{\mathbf{D}}(\mathbf{n}^i, \mathbf{m}^i) \mathbf{M}(\tilde{\mathbf{n}}^i) \tag{90}$$

where $\bar{\mathbf{D}}(\mathbf{n}^i, \mathbf{m}^i)$ is the effective constitutive matrix in LCS ($\mathbf{n}^i, \mathbf{m}^i$) and can be computed by Equation (45). $\mathbf{M}(\tilde{\mathbf{n}}^i)$ is the transform matrix corresponding to the direction $\tilde{\mathbf{n}}^i$ and

$$\tilde{\mathbf{n}}^i = \vartheta \mathbf{n}^i + (1\text{-}\vartheta) \tilde{\mathbf{n}}^{i-1} \tag{91}$$

where $\mathbf{n}^i$ is the direction computed by the unified failure criterion at iteration step i, and $\vartheta \in (0,1]$ is a weight parameter. In this paper, $\vartheta = 1$ is applied in most cases. However, Equation (84) may not converge to a given residual if χ^2 is close to 0.5 in some cases. In this situation, a smaller $\vartheta \in (0, 0.5]$ can be implemented to improve the convergence.

The non-linear system of equations obtained by Equation (85) can be solved by Newton's method. In the real implementation, we have found out that both inner iterations for solving Equations (84) and (85) are not needed in most cases.

6. Numerical examples

In this section, some numerical examples are proposed to show the ability of the proposed model in mixed-mode fracture modeling. Plane stress states and the linear softening law are assumed in the examples if not specified, and the direct displacement control is applied in the simulation. The initial crack is modeled as discrete discontinuity in the geometry. In all the examples, the staggered scheme with iterations, i.e., the alternate minimization algorithm [16] is applied to solve the model if not specified. Both inner iterations for solving Equations (84) and (85) are not performed in the alternate minimization algorithm, i.e., only the outer iterations between Equations (84) and (85) are performed and the scheme will be stopped if the L2-norm of the phase-field between two consecutive iteration steps is below 10^{-5}.

6.1 2D bar under tensional loading

A 2D bar with length $L = 4$mm and height $H = 1$mm under tensional loading shown in Figure 5 is tested and the material properties are Young's modulus $E = 200$GPa, Poisson's ratio $\nu = 0.3$, fracture energy $G_c^t = 10$N/mm, and failure tension strength $f_t = 0.25$ GPa. A total of 40,000 uniform structured quadrilateral elements (the mesh size is 0.01mm) are used to discretize the domain and two length scales $l_0 = 0.05$ mm and $l_0 = 0.10$ mm are applied in all the examples. The crack path may form at the left boundary edge because the stresses at points near the left edge are higher than those near the right edge since the left edge is fully fixed. Thus, the Dirichlet condition $s = 0$ is imposed on both left and right edges [26, 52], and no initial defects are introduced in the simulation.

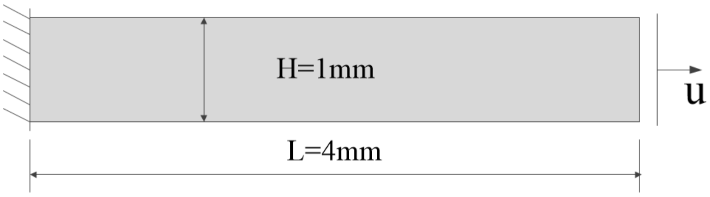

Figure 5. The bar under tensional loading: Geometry and boundary conditions

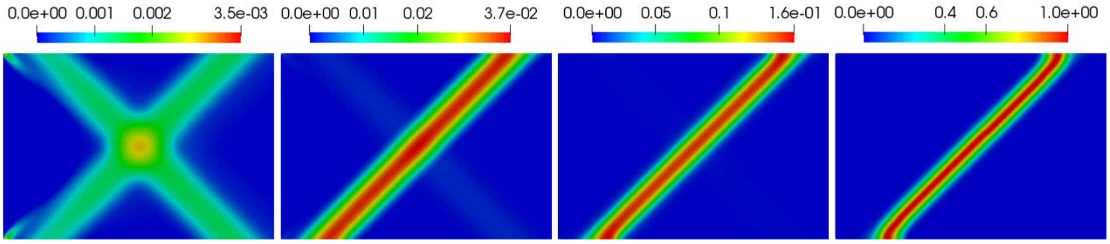

(a) u=0.0055mm (χ=0.01) (b) u=0.01mm (χ=0.01) (c) u=0.02mm (χ=0.01) (d) u=0.2mm (χ=0.01)

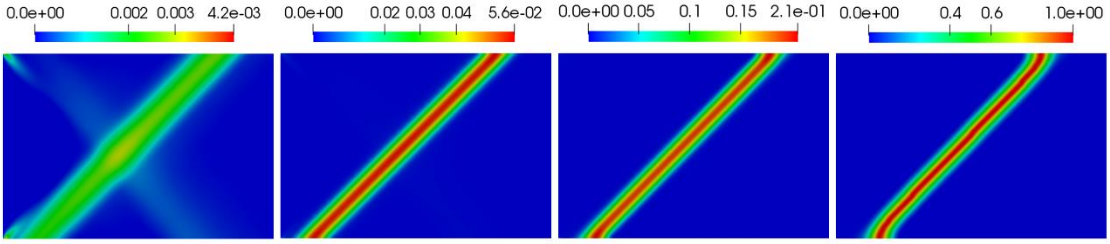

(e) u=0.0055mm (χ=0.3) (f) u=0.01mm (χ=0.3) (g) u=0.02mm (χ=0.3) (h) u=0.2mm (χ=0.3)

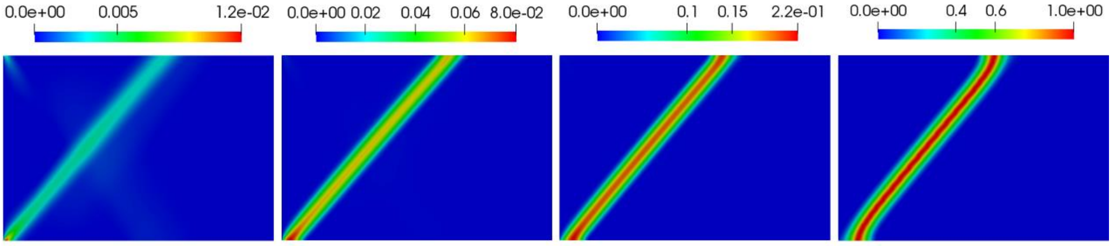

(i) u=0.0055mm (χ=0.55) (j) u=0.01mm (χ=0.55) (k) u=0.02mm (χ=0.55) (l) u=0.2mm (χ=0.55)

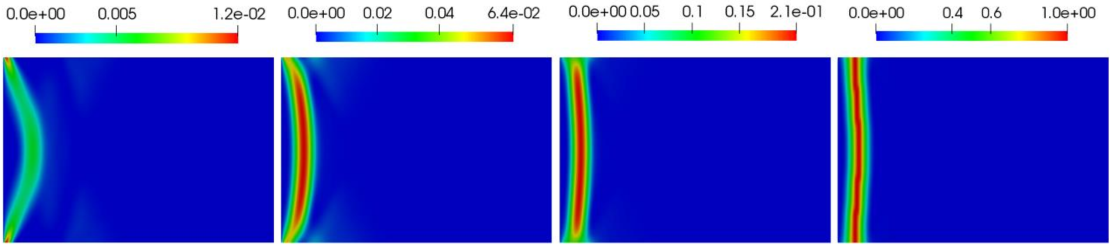

(m) u=0.0055mm (χ=10) (n) u=0.01mm (χ=10) (o) u=0.02mm (χ=10) (p) u=0.2mm (χ=10)

Figure 6. Crack initiations for the bar under tensional loading (l_0=0.05mm, n=0.5)

Several different values of $\chi = \tau_s / \sigma_t$ are considered in the simulation. The displacement increment Δu is 0.004 mm in the first step, and $\Delta u = 10^{-4}$ mm is used for the 2nd to 100th steps, then $\Delta u = 10^{-3}$ mm is applied for the rest steps. Different values of n in functions b_I and b_{II} shown in Equation (82) are tested, and the crack initiations for length scales $l_0 = 0.05$ mm with n=0.5, i.e., $b_I = \cos^{0.5}(2\theta)$, $b_{II} = \sin^{0.5}(2\theta)$ are shown in Figure 6. All the cracks initiate near the left edge since the left edge is fully fixed. The final crack paths at displacement u=0.2 mm are shown in Figure 7, Figure 8, Figure 9, and Figure 10 for χ =0.01, 0.3, 0.55, and 10.0, respectively. It can be observed that different fracture angles are obtained by changing χ. In the special cases $\chi \to 0$ and $\chi^2 > 0.5$, the fracture angles are $\theta_T \to \pi / 4$ and $\theta_T = \pi / 2$, respectively, which can be reproduced by the proposed numerical model (see Figure 7 and Figure 10). The hybrid model with $b_I = b_{II} = 1.0$ can also obtain $\theta_T = \pi / 2$ for the case $\chi^2 > 0.5$ (see Figure 10). However, it cannot obtain $\theta_T \to \pi / 4$ for the case $\chi \to 0$ in this numerical example (see Figure 7(d) and Figure 7(h)). The fracture angle θ_T increases as the values of n in both b_I and b_{II} decrease, and the hybrid model can be considered as $n = 0$. One can also observe that the length scale has little influence on the crack paths for all the examples, except that the crack bandwidth is wider when $l_0 = 0.10$ mm.

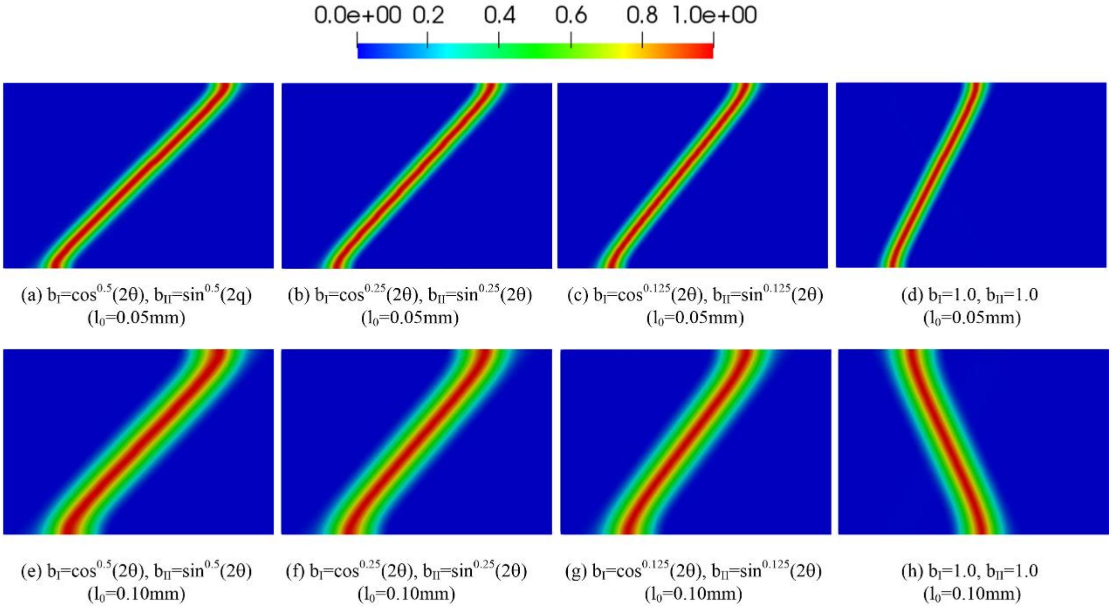

(a) $b_I=\cos^{0.5}(2\theta)$, $b_{II}=\sin^{0.5}(2q)$ (l_0=0.05mm)

(b) $b_I=\cos^{0.25}(2\theta)$, $b_{II}=\sin^{0.25}(2\theta)$ (l_0=0.05mm)

(c) $b_I=\cos^{0.125}(2\theta)$, $b_{II}=\sin^{0.125}(2\theta)$ (l_0=0.05mm)

(d) b_I=1.0, b_{II}=1.0 (l_0=0.05mm)

(e) $b_I=\cos^{0.5}(2\theta)$, $b_{II}=\sin^{0.5}(2\theta)$ (l_0=0.10mm)

(f) $b_I=\cos^{0.25}(2\theta)$, $b_{II}=\sin^{0.25}(2\theta)$ (l_0=0.10mm)

(g) $b_I=\cos^{0.125}(2\theta)$, $b_{II}=\sin^{0.125}(2\theta)$ (l_0=0.10mm)

(h) b_I=1.0, b_{II}=1.0 (l_0=0.10mm)

Figure 7. Crack paths for the bar under tensional loading (χ =0.01)

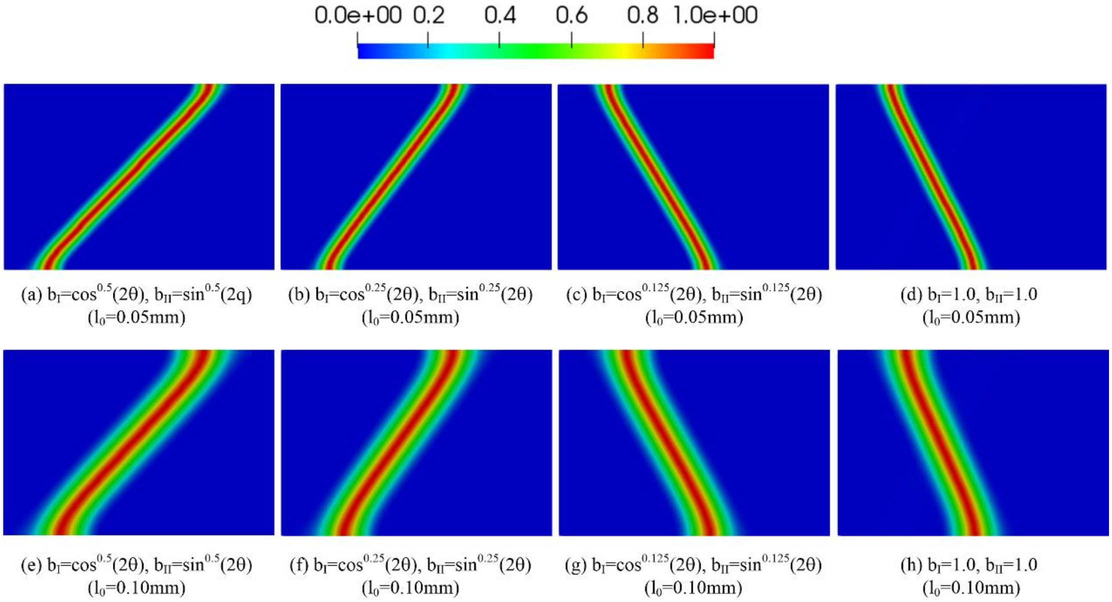

(a) $b_I=\cos^{0.5}(2\theta)$, $b_{II}=\sin^{0.5}(2q)$ (l_0=0.05mm)

(b) $b_I=\cos^{0.25}(2\theta)$, $b_{II}=\sin^{0.25}(2\theta)$ (l_0=0.05mm)

(c) $b_I=\cos^{0.125}(2\theta)$, $b_{II}=\sin^{0.125}(2\theta)$ (l_0=0.05mm)

(d) b_I=1.0, b_{II}=1.0 (l_0=0.05mm)

(e) $b_I=\cos^{0.5}(2\theta)$, $b_{II}=\sin^{0.5}(2\theta)$ (l_0=0.10mm)

(f) $b_I=\cos^{0.25}(2\theta)$, $b_{II}=\sin^{0.25}(2\theta)$ (l_0=0.10mm)

(g) $b_I=\cos^{0.125}(2\theta)$, $b_{II}=\sin^{0.125}(2\theta)$ (l_0=0.10mm)

(h) b_I=1.0, b_{II}=1.0 (l_0=0.10mm)

Figure 8. Crack paths for the bar under tensional loading (χ =0.3)

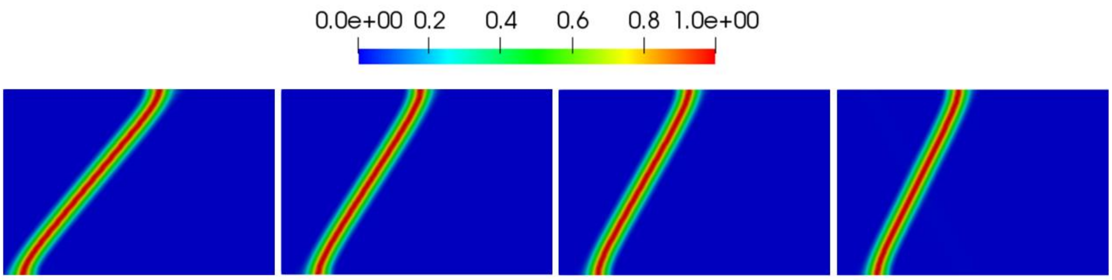

(a) $b_I=\cos^{0.5}(2\theta)$, $b_{II}=\sin^{0.5}(2q)$ (l_0=0.05mm)
(b) $b_I=\cos^{0.25}(2\theta)$, $b_{II}=\sin^{0.25}(2\theta)$ (l_0=0.05mm)
(c) $b_I=\cos^{0.125}(2\theta)$, $b_{II}=\sin^{0.125}(2\theta)$ (l_0=0.05mm)
(d) b_I=1.0, b_{II}=1.0 (l_0=0.05mm)

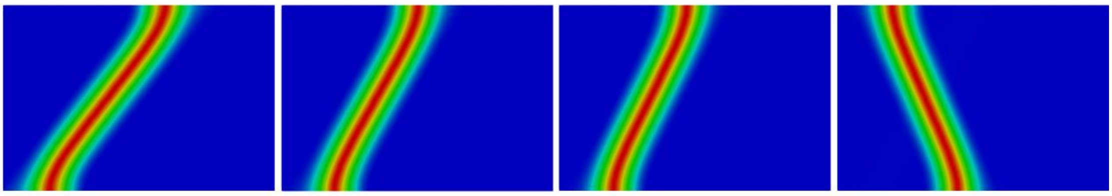

(e) $b_I=\cos^{0.5}(2\theta)$, $b_{II}=\sin^{0.5}(2\theta)$ (l_0=0.10mm)
(f) $b_I=\cos^{0.25}(2\theta)$, $b_{II}=\sin^{0.25}(2\theta)$ (l_0=0.10mm)
(g) $b_I=\cos^{0.125}(2\theta)$, $b_{II}=\sin^{0.125}(2\theta)$ (l_0=0.10mm)
(h) b_I=1.0, b_{II}=1.0 (l_0=0.10mm)

Figure 9. Crack paths for the bar under tensional loading (χ =0.55)

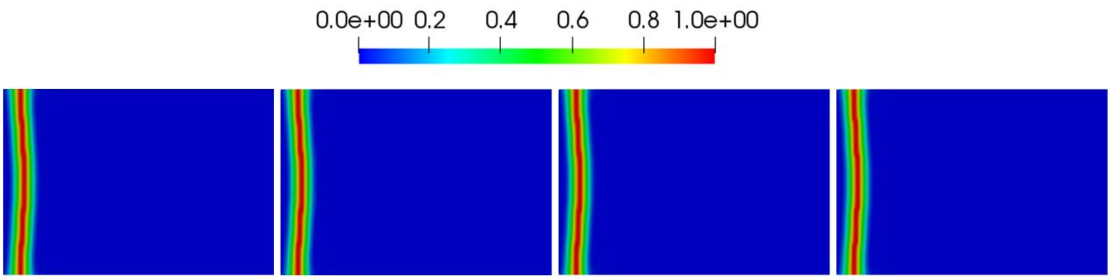

(a) $b_I=\cos^{0.5}(2\theta)$, $b_{II}=\sin^{0.5}(2q)$ (l_0=0.05mm)
(b) $b_I=\cos^{0.25}(2\theta)$, $b_{II}=\sin^{0.25}(2\theta)$ (l_0=0.05mm)
(c) $b_I=\cos^{0.125}(2\theta)$, $b_{II}=\sin^{0.125}(2\theta)$ (l_0=0.05mm)
(d) b_I=1.0, b_{II}=1.0 (l_0=0.05mm)

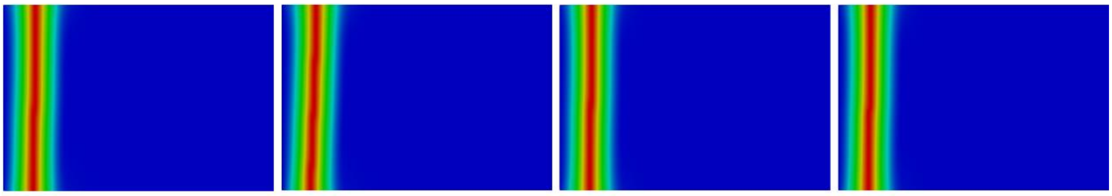

(e) $b_I=\cos^{0.5}(2\theta)$, $b_{II}=\sin^{0.5}(2\theta)$ (l_0=0.10mm)
(f) $b_I=\cos^{0.25}(2\theta)$, $b_{II}=\sin^{0.25}(2\theta)$ (l_0=0.10mm)
(g) $b_I=\cos^{0.125}(2\theta)$, $b_{II}=\sin^{0.125}(2\theta)$ (l_0=0.10mm)
(h) b_I=1.0, b_{II}=1.0 (l_0=0.10mm)

Figure 10. Crack paths for the bar under tensional loading (χ =10.0)

One can also observe that the directions of crack paths for some cases are distinct from others, for example, the crack path shown in Figure 7(h) is from the left upper corner to the right lower corner, while the others in Figure 7 are from the left lower corner to the right upper corner. The “X” shape crack path can be observed at the beginning of crack initiation (see Figure 6(a)), and one crack will become the major crack because of the computational error in the simulation. Thus, both the crack directions shown in Figure 7(d) and Figure 7(h) may be observed. The load-displacement curves are shown in Figure 11, and all the maximum loadings are close to 0.25 kN because the given failure tension strength is fixed. Actually, both the mesh size and length scale have very little influence on the load-displacement curves [52].

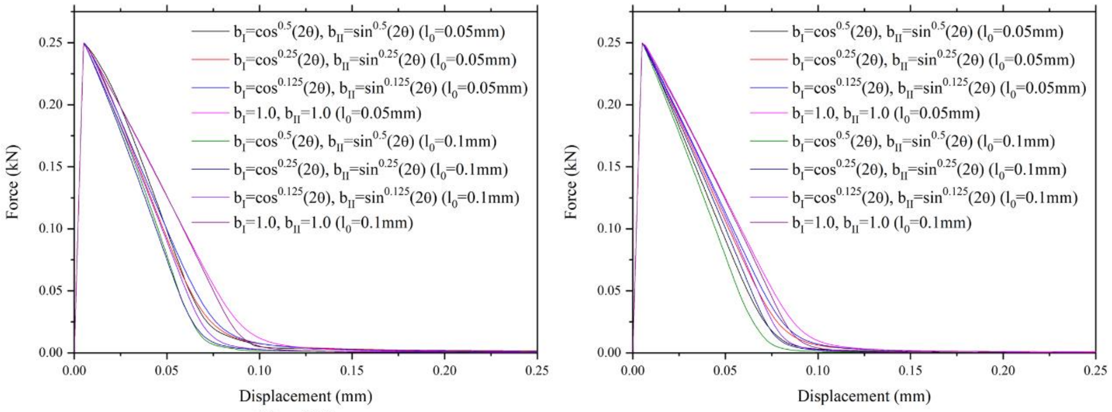

(a) χ=0.01 (b) χ=0.3

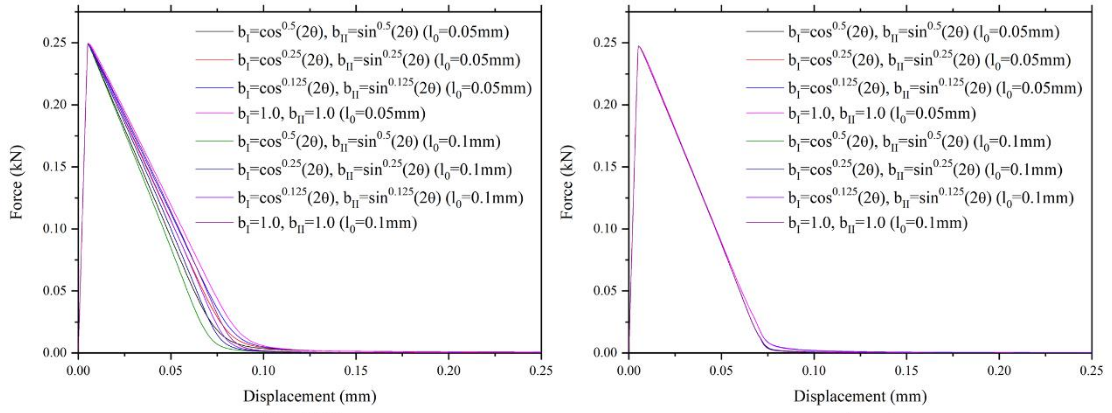

(c) χ=0.55 (d) χ=10

Figure 11. Load-displacement curves for the bar under tensional loading

6.2 Single-edge notched plate under shear

A plate with a notch shown in Figure 12 is considered in this example. The lengths of the plate and notch are 1.0mm and 0.5mm, respectively. The bottom edge is fixed and a horizontal displacement is imposed on the upper edge. Especially, the vertical displacements are fixed to zero on all the boundaries. The material properties are [27, 52]: Young's modulus $E=210$ GPa, Poisson's ratio $\nu=0.3$, fracture energy $G_c^t=2.7$ N/mm, and failure tension strength $f_t=2445$ MPa. Four different $\chi=0.0001$, 0.3, 0.6, and 1.0 are tested. In all the simulations, 158, 404 uniform structured quadrilateral elements (the mesh size is about 0.0025mm) are applied to discretize the domain and the length scale is $l_0=0.01$mm. The displacement increment Δu is 10^{-4} mm and four different functions of b_I and b_{II} are tested.

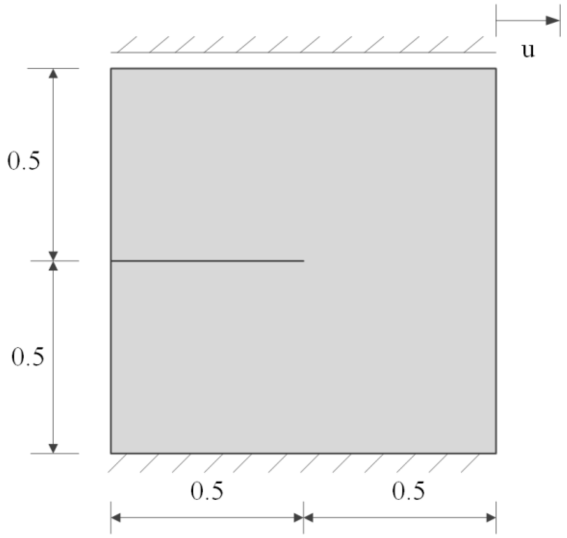

Figure 12. Single-edge notched plate under shear (unit: mm)

The crack paths obtained by the proposed phase-field model are shown in Figure 13(a-d), Figure 14(a-d), Figure 15(a-d), and Figure 16(a-d). It can be observed that the crack paths for the case $\chi = 0.0001$ are close to horizontal lines, which are close to the theoretical results of the pure shear test. However, this crack path is still an inclined line (see Figure 13(a-d) and Figure 14(a-d)), and the main reason is that some elements may be under compression, i.e., $\bar{\sigma}_1 + \bar{\sigma}_2 < 0$, because of the computational round-off error. Thus, a modified crack direction search algorithm can be applied for the case $\bar{\sigma}_1 + \bar{\sigma}_2 < 0$ as:

(i) If $\bar{\sigma}_1 + \bar{\sigma}_2 < 0$ and $\bar{\sigma}_1 / \sigma_t > (\bar{\sigma}_1 - \bar{\sigma}_2) / (2\tau_s)$, $\theta = 0$ (see Figure 17(a));

(ii) If $\bar{\sigma}_1 + \bar{\sigma}_2 < 0$ and $\bar{\sigma}_1 / \sigma_t \le (\bar{\sigma}_1 - \bar{\sigma}_2) / (2\tau_s)$, $\theta = \pi / 4$ (see Figure 17(b)).

(iii) if $\bar{\sigma}_1 < 0$, $\theta = \pi / 4$, $\psi_{0II}^{+} = \bar{\tau}^2 / (2\mu)$.

The original crack direction search algorithm is called *method 1*, and the modified crack direction search algorithm can be called *method 2*. The crack paths obtained by the modified crack direction search algorithm (method 2) are shown in Figure 13(e-h), Figure 14(e-h), Figure 15(e-h), and Figure 16(e-h). It can be observed that the crack path for the case $\chi = 0.0001$ is a horizontal line now, which is closer to the theoretical result. The crack paths for the case $\chi = 0.3$ are also flatter than those obtained by the original direction search algorithm (i.e., method 1). One can also observe that different b_I and b_2 have very little influence on the crack paths in this example.

The load-displacement curves are shown in Figure 18. The peak force increases with the increase of χ for cases $\chi = 0.0001$, 0.3 and 0.5, and the peak forces obtained by method 1 are close to those obtained by method 2, especially for cases $\chi = 0.0001$ and 1.0. One can also observe that different values of *n* used in b_I and b_{II} have no much influence on the load-displacement curves.

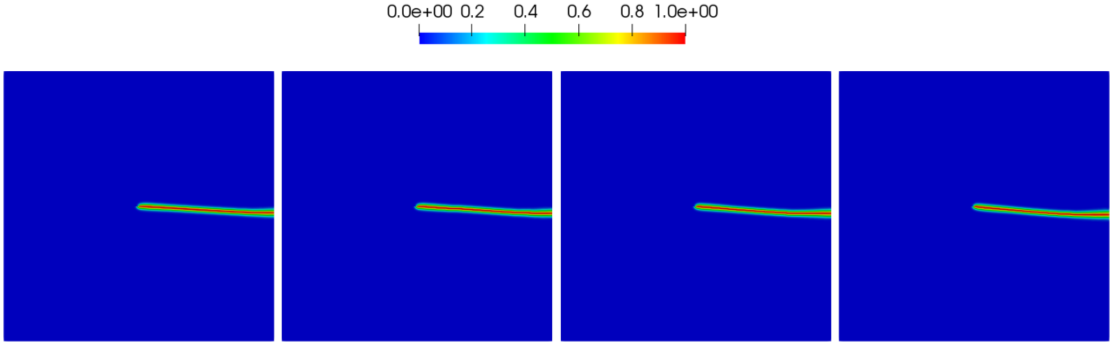

(a) $b_I=\cos^{0.5}(2\theta)$, $b_{II}=\sin^{0.5}(2\theta)$ (method 1) (b) $b_I=\cos^{0.25}(2\theta)$, $b_{II}=\sin^{0.25}(2\theta)$ (method 1) (c) $b_I=\cos^{0.125}(2\theta)$, $b_{II}=\sin^{0.125}(2\theta)$ (method 1) (d) $b_I=1.0$, $b_{II}=1.0$ (method 1)

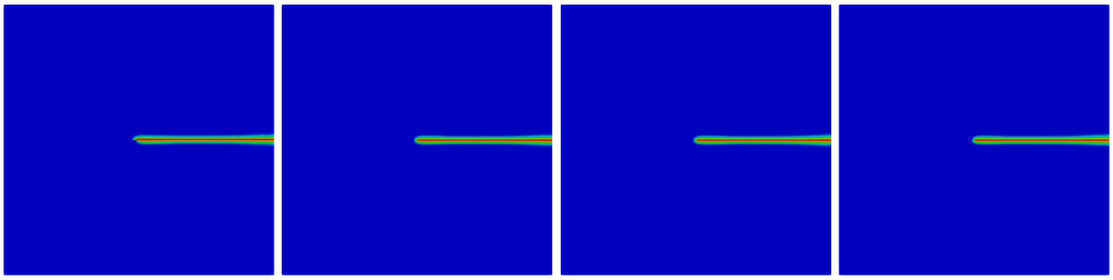

(c) $b_I=\cos^{0.5}(2\theta)$, $b_{II}=\sin^{0.5}(2\theta)$ (method 2) (f) $b_I=\cos^{0.25}(2\theta)$, $b_{II}=\sin^{0.25}(2\theta)$ (method 2) (g) $b_I=\cos^{0.125}(2\theta)$, $b_{II}=\sin^{0.125}(2\theta)$ (method 2) (h) $b_I=1.0$, $b_{II}=1.0$ (method 2)

Figure 13. Crack paths for the single-edge notched plate under shear (χ =0.001)

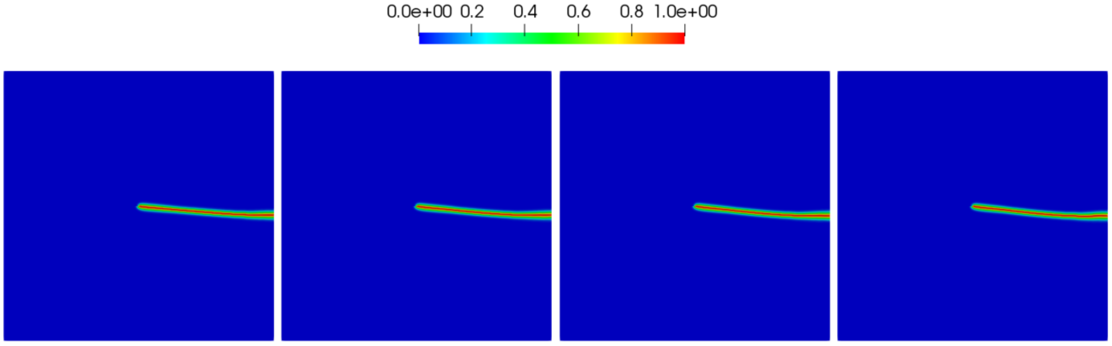

(a) $b_I=\cos^{0.5}(2\theta)$, $b_{II}=\sin^{0.5}(2\theta)$ (method 1) (b) $b_I=\cos^{0.25}(2\theta)$, $b_{II}=\sin^{0.25}(2\theta)$ (method 1) (c) $b_I=\cos^{0.125}(2\theta)$, $b_{II}=\sin^{0.125}(2\theta)$ (method 1) (d) $b_I=1.0$, $b_{II}=1.0$ (method 1)

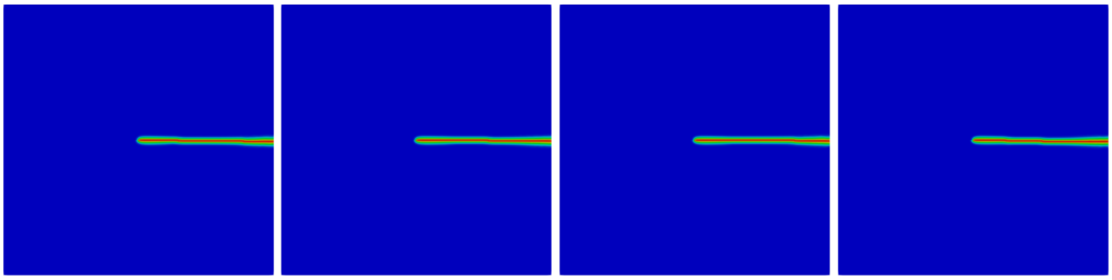

(c) $b_I=\cos^{0.5}(2\theta)$, $b_{II}=\sin^{0.5}(2\theta)$ (method 2) (f) $b_I=\cos^{0.25}(2\theta)$, $b_{II}=\sin^{0.25}(2\theta)$ (method 2) (g) $b_I=\cos^{0.125}(2\theta)$, $b_{II}=\sin^{0.125}(2\theta)$ (method 2) (h) $b_I=1.0$, $b_{II}=1.0$ (method 2)

Figure 14. Crack paths for the single-edge notched plate under shear (χ =0.3)

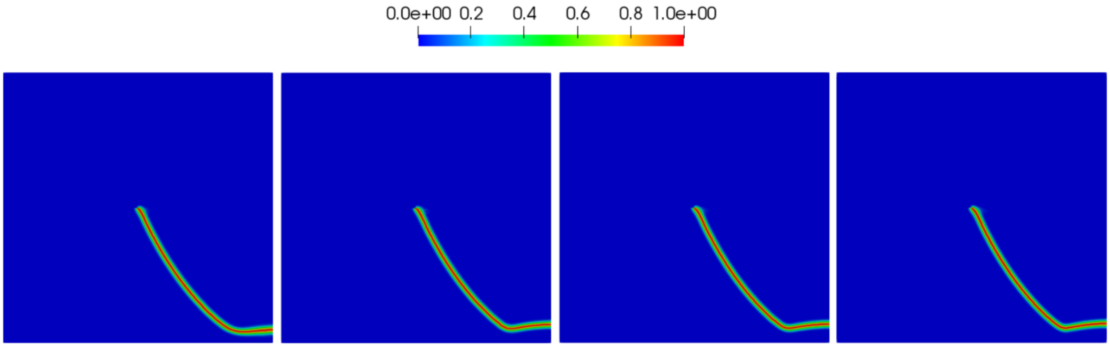

(a) $b_I=\cos^{0.5}(2\theta)$, $b_{II}=\sin^{0.5}(2\theta)$ (method 1)

(b) $b_I=\cos^{0.25}(2\theta)$, $b_{II}=\sin^{0.25}(2\theta)$ (method 1)

(c) $b_I=\cos^{0.125}(2\theta)$, $b_{II}=\sin^{0.125}(2\theta)$ (method 1)

(d) $b_I=1.0$, $b_{II}=1.0$ (method 1)

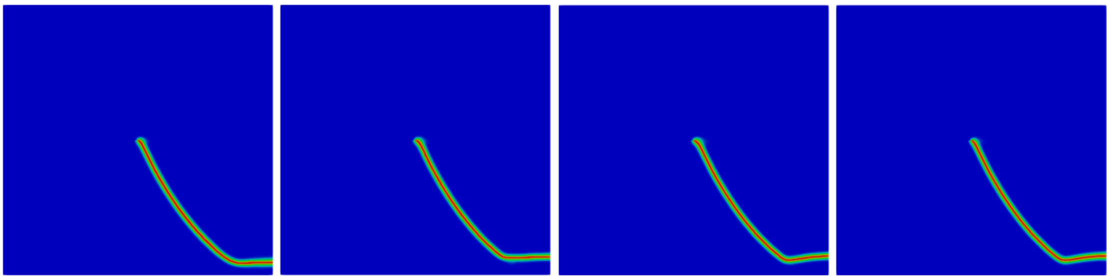

(e) $b_I=\cos^{0.5}(2\theta)$, $b_{II}=\sin^{0.5}(2\theta)$ (method 2)

(f) $b_I=\cos^{0.25}(2\theta)$, $b_{II}=\sin^{0.25}(2\theta)$ (method 2)

(g) $b_I=\cos^{0.125}(2\theta)$, $b_{II}=\sin^{0.125}(2\theta)$ (method 2)

(h) $b_I=1.0$, $b_{II}=1.0$ (method 2)

Figure 15. Crack paths for the single-edge notched plate under shear (χ =0.6)

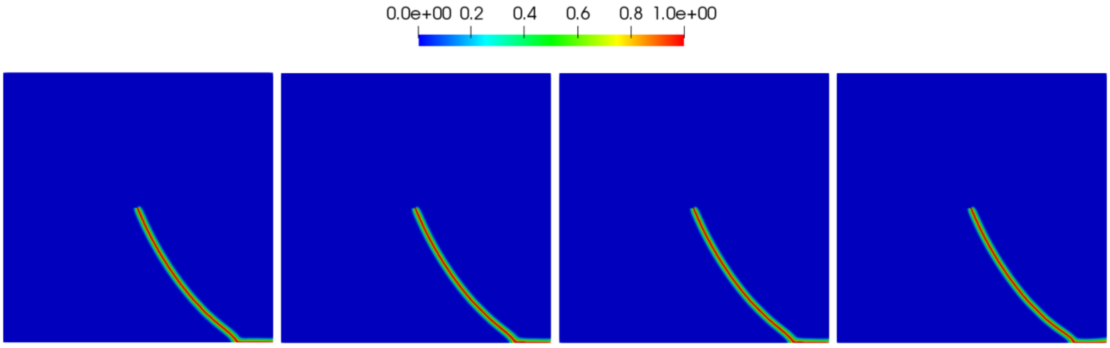

(a) $b_I=\cos^{0.5}(2\theta)$, $b_{II}=\sin^{0.5}(2\theta)$ (method 1)

(b) $b_I=\cos^{0.25}(2\theta)$, $b_{II}=\sin^{0.25}(2\theta)$ (method 1)

(c) $b_I=\cos^{0.125}(2\theta)$, $b_{II}=\sin^{0.125}(2\theta)$ (method 1)

(d) $b_I=1.0$, $b_{II}=1.0$ (method 1)

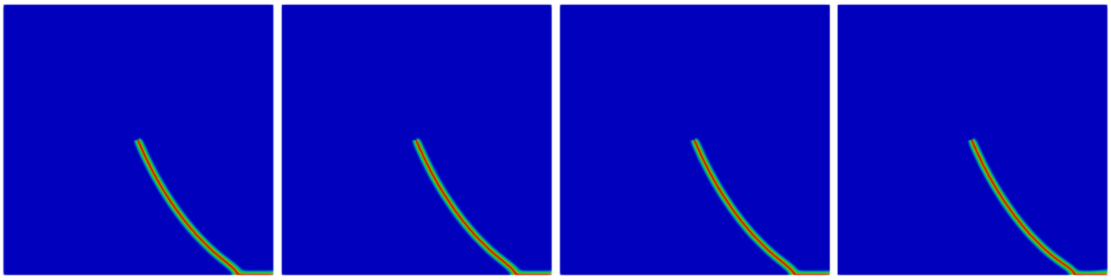

(e) $b_I=\cos^{0.5}(2\theta)$, $b_{II}=\sin^{0.5}(2\theta)$ (method 2)

(f) $b_I=\cos^{0.25}(2\theta)$, $b_{II}=\sin^{0.25}(2\theta)$ (method 2)

(g) $b_I=\cos^{0.125}(2\theta)$, $b_{II}=\sin^{0.125}(2\theta)$ (method 2)

(h) $b_I=1.0$, $b_{II}=1.0$ (method 2)

Figure 16. Crack paths for the single-edge notched plate under shear (χ =1.0)

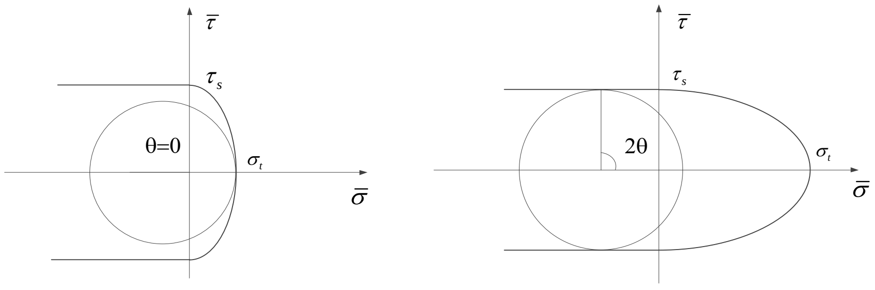

(a) $\bar{\sigma}_1+\bar{\sigma}_2<0,\quad \bar{\sigma}_1/\sigma_t>(\bar{\sigma}_1-\bar{\sigma}_2)/(2\tau_s)$

(b) $\bar{\sigma}_1+\bar{\sigma}_2<0, \bar{\sigma}_1/\sigma_t\le(\bar{\sigma}_1-\bar{\sigma}_2)/(2\tau_s)$

Figure 17. The modified crack direction search algorithm for $\bar{\sigma}_1+\bar{\sigma}_2<0$.

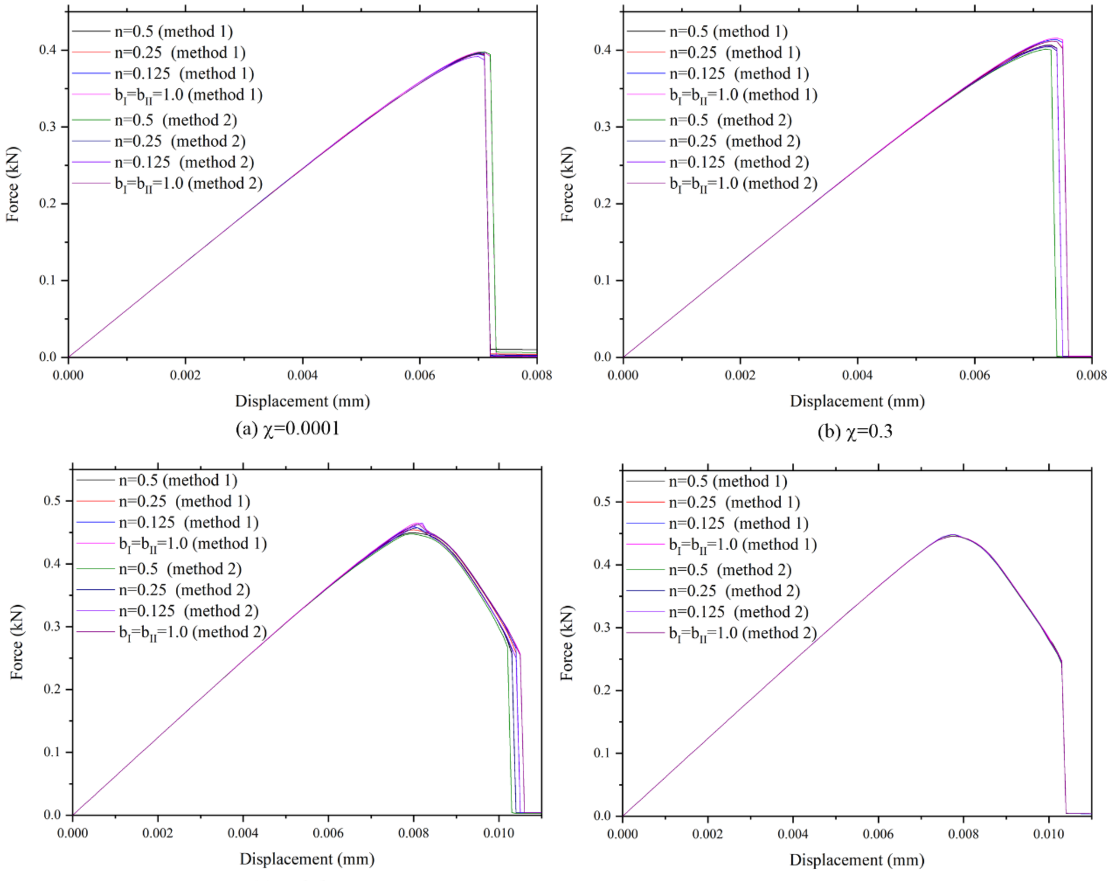

(a) χ=0.0001 (b) χ=0.3

(c) χ=0.6 (d) χ=1.0

Figure 18. Load-displacement curves for the single-edge notched plate under shear

6.3 Single-inclined notched plate under tension

A single-inclined notched plate under tension shown in Figure 19 is studied in this example. The length of the plate is 1.0mm and the notch is located in the center of the plate (see Figure 19(a)). A total of 122,606 triangular elements are used to discretize the domain with fine meshes (the mesh size is about 0.003mm) assigned to the critical zones (see Figure 19(b)) and two length scales l_0 =0.006 and 0.012 mm are applied. The material properties are Young's modulus $E=210$ GPa, Poisson's ratio $\nu=0.3$, fracture energy $G_c^t=5.0$ N/mm, and failure tension strength $f_t=2000$

MPa. Four different χ=0.1, 0.25, 0.4, and 10 are considered. The displacement increment Δu is 10^{-4} mm in all the examples.

The crack paths obtained by different χ are shown in Figure 20, Figure 21, Figure 22, and Figure 23, respectively. As expected, different crack paths are obtained according to the mixed-mode phase-field model. One can also observe that different b_I and b_{II} have a slight influence on the crack paths, and the length scale only influences the crack bandwidth. The load-displacement curves are shown in Figure 24. One can also find out that the peak force decreases with the increase of χ in this example. The mesh size $h=(\frac{1}{4}\sim\frac{1}{2})\,l_0$ is used in these examples and the desired crack patters can be obtained. To obtain more accurate results, such as the fracture surface energy, the mesh size h should be sufficiently small compared to the length scale l_0, and $h=(\frac{1}{10}\sim\frac{1}{5})\,l_0$ is suggested in the unified phase-field theory [26, 52].

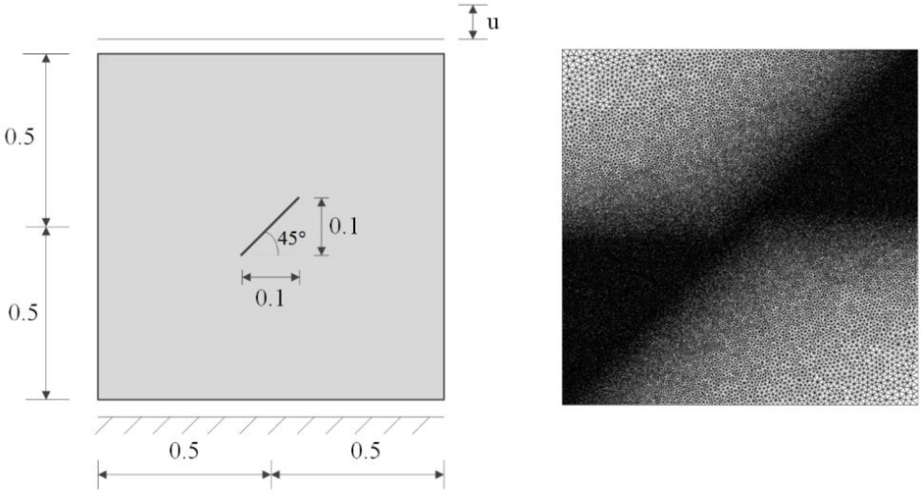

(a) Geometry and boundary conditions

(b) Mesh

Figure 19. Single-inclined notched plate under tension (unit: mm)

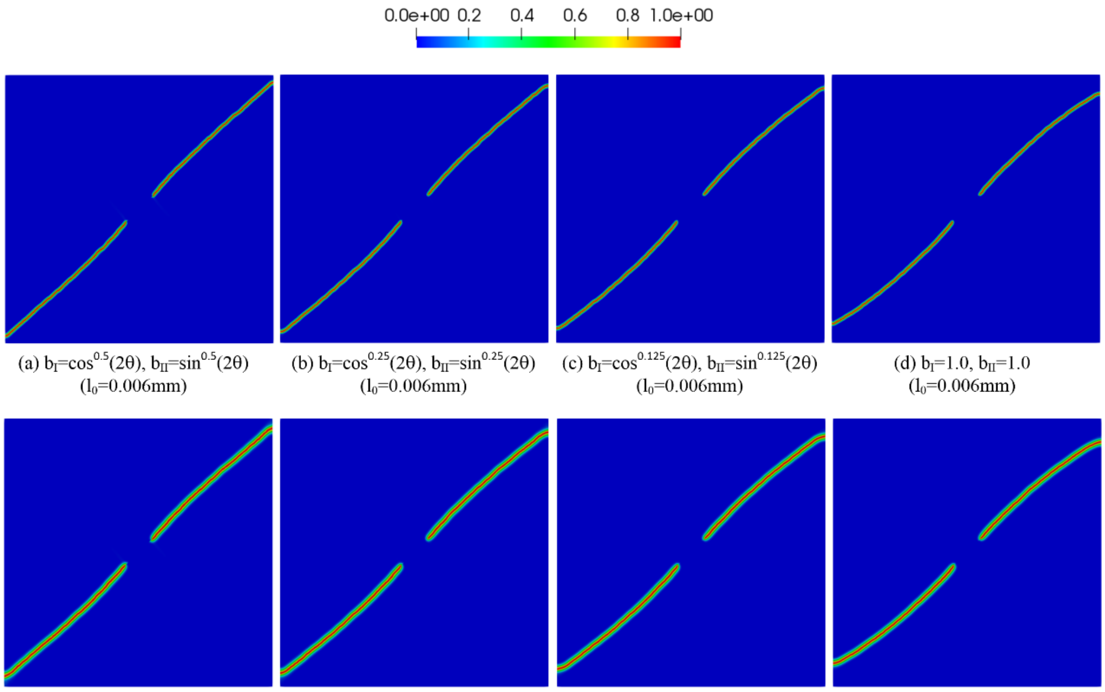

(a) $b_I=\cos^{0.5}(2\theta)$, $b_{II}=\sin^{0.5}(2\theta)$ ($l_0=0.006$mm)

(b) $b_I=\cos^{0.25}(2\theta)$, $b_{II}=\sin^{0.25}(2\theta)$ ($l_0=0.006$mm)

(c) $b_I=\cos^{0.125}(2\theta)$, $b_{II}=\sin^{0.125}(2\theta)$ ($l_0=0.006$mm)

(d) $b_I=1.0$, $b_{II}=1.0$ ($l_0=0.006$mm)

(e) $b_I=\cos^{0.5}(2\theta)$, $b_{II}=\sin^{0.5}(2\theta)$ ($l_0=0.012$mm)

(f) $b_I=\cos^{0.25}(2\theta)$, $b_{II}=\sin^{0.25}(2\theta)$ ($l_0=0.012$mm)

(g) $b_I=\cos^{0.125}(2\theta)$, $b_{II}=\sin^{0.125}(2\theta)$ ($l_0=0.012$mm)

(h) $b_I=1.0$, $b_{II}=1.0$ ($l_0=0.012$mm)

Figure 20. Crack paths for the single-inclined notched plate under tension ($\chi=0.1$)

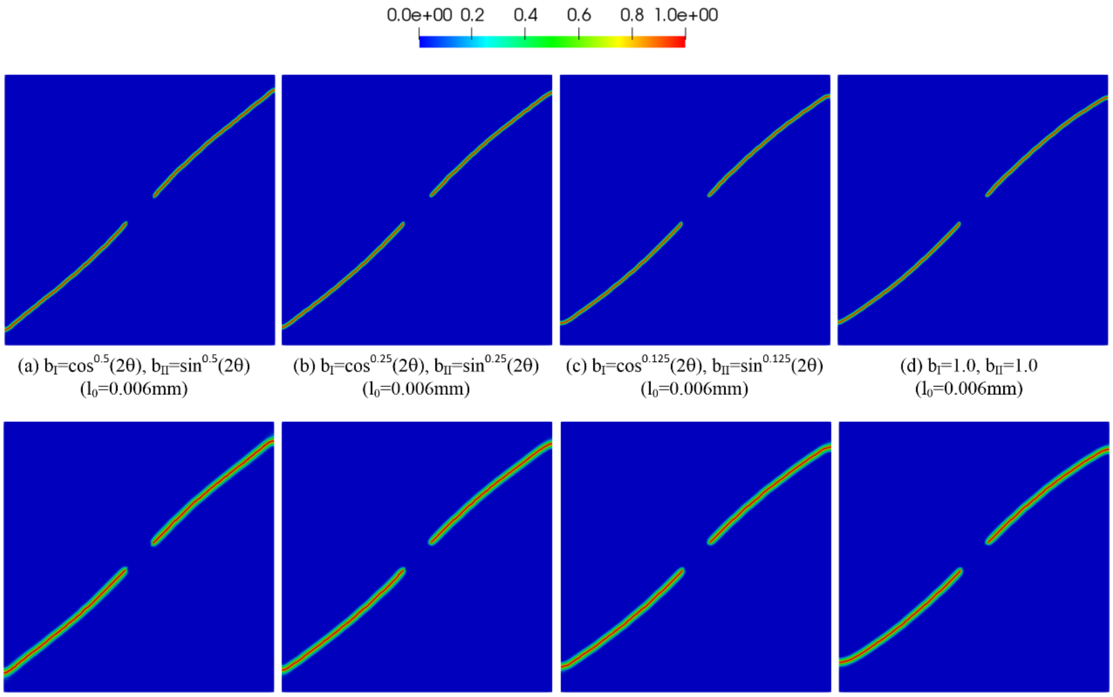

(a) $b_I=\cos^{0.5}(2\theta)$, $b_{II}=\sin^{0.5}(2\theta)$ ($l_0=0.006$mm)

(b) $b_I=\cos^{0.25}(2\theta)$, $b_{II}=\sin^{0.25}(2\theta)$ ($l_0=0.006$mm)

(c) $b_I=\cos^{0.125}(2\theta)$, $b_{II}=\sin^{0.125}(2\theta)$ ($l_0=0.006$mm)

(d) $b_I=1.0$, $b_{II}=1.0$ ($l_0=0.006$mm)

(e) $b_I=\cos^{0.5}(2\theta)$, $b_{II}=\sin^{0.5}(2\theta)$ ($l_0=0.012$mm)

(f) $b_I=\cos^{0.25}(2\theta)$, $b_{II}=\sin^{0.25}(2\theta)$ ($l_0=0.012$mm)

(g) $b_I=\cos^{0.125}(2\theta)$, $b_{II}=\sin^{0.125}(2\theta)$ ($l_0=0.012$mm)

(h) $b_I=1.0$, $b_{II}=1.0$ ($l_0=0.012$mm)

Figure 21. Crack paths for the single-inclined notched plate under tension ($\chi=0.25$)

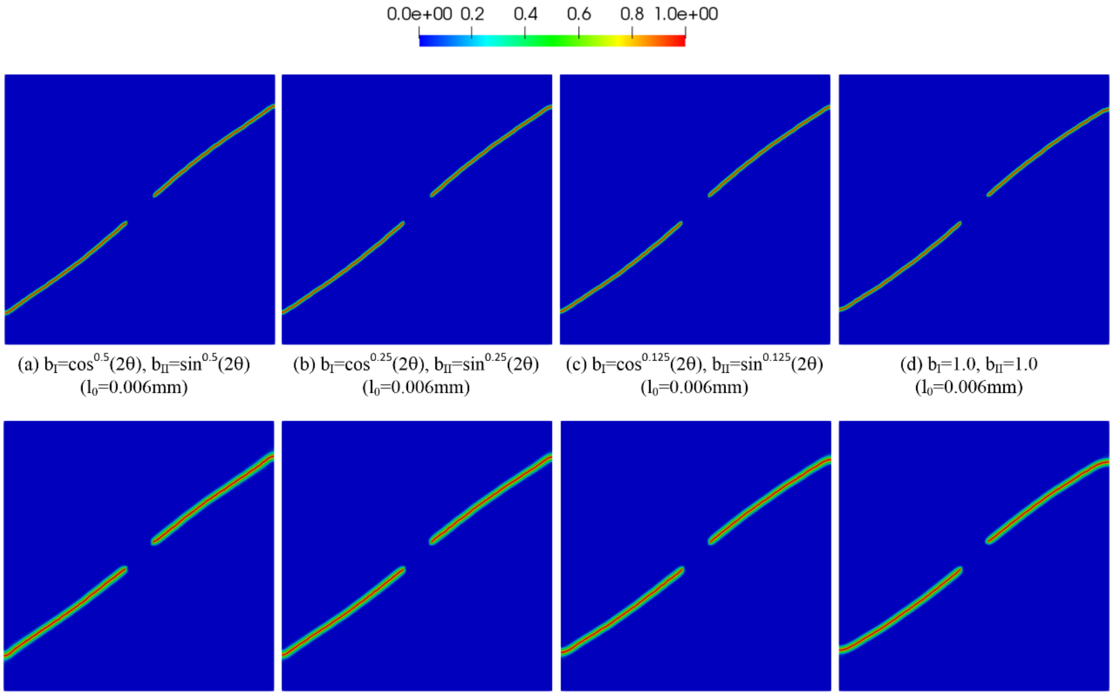

(a) $b_I=\cos^{0.5}(2\theta)$, $b_{II}=\sin^{0.5}(2\theta)$ (l_0=0.006mm)

(b) $b_I=\cos^{0.25}(2\theta)$, $b_{II}=\sin^{0.25}(2\theta)$ (l_0=0.006mm)

(c) $b_I=\cos^{0.125}(2\theta)$, $b_{II}=\sin^{0.125}(2\theta)$ (l_0=0.006mm)

(d) b_I=1.0, b_{II}=1.0 (l_0=0.006mm)

(c) $b_I=\cos^{0.5}(2\theta)$, $b_{II}=\sin^{0.5}(2\theta)$ (l_0=0.012mm)

(f) $b_I=\cos^{0.25}(2\theta)$, $b_{II}=\sin^{0.25}(2\theta)$ (l_0=0.012mm)

(g) $b_I=\cos^{0.125}(2\theta)$, $b_{II}=\sin^{0.125}(2\theta)$ (l_0=0.012mm)

(h) b_I=1.0, b_{II}=1.0 (l_0=0.012mm)

Figure 22. Crack paths for the single-inclined notched plate under tension (χ=0.4)

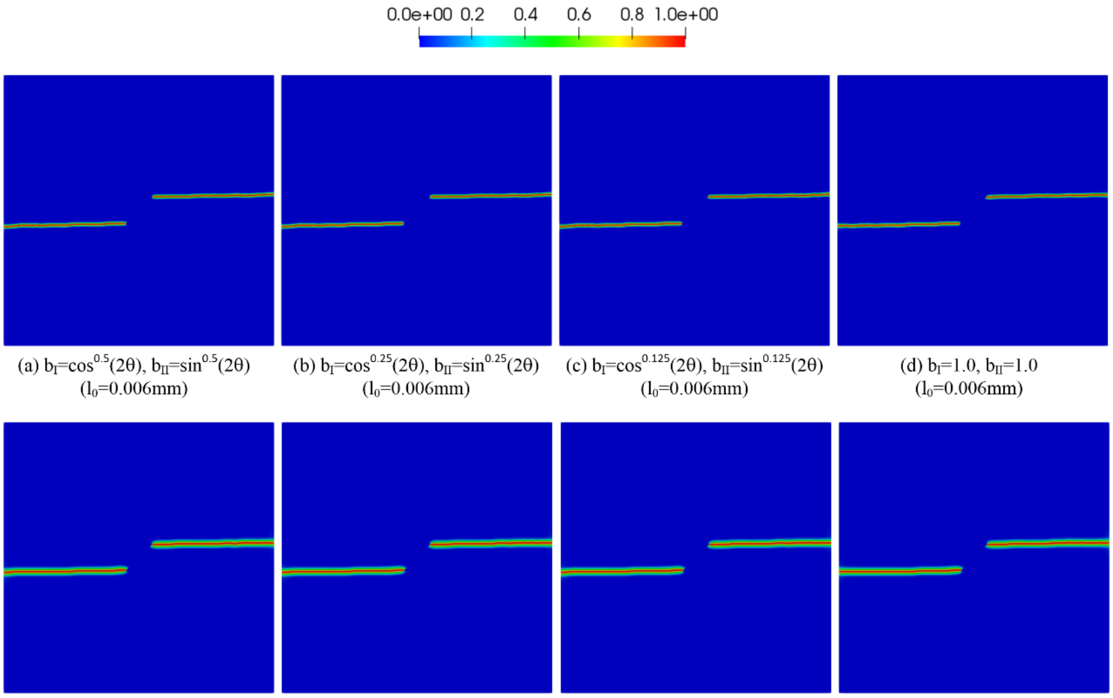

(a) $b_I=\cos^{0.5}(2\theta)$, $b_{II}=\sin^{0.5}(2\theta)$ (l_0=0.006mm)

(b) $b_I=\cos^{0.25}(2\theta)$, $b_{II}=\sin^{0.25}(2\theta)$ (l_0=0.006mm)

(c) $b_I=\cos^{0.125}(2\theta)$, $b_{II}=\sin^{0.125}(2\theta)$ (l_0=0.006mm)

(d) b_I=1.0, b_{II}=1.0 (l_0=0.006mm)

(c) $b_I=\cos^{0.5}(2\theta)$, $b_{II}=\sin^{0.5}(2\theta)$ (l_0=0.012mm)

(f) $b_I=\cos^{0.25}(2\theta)$, $b_{II}=\sin^{0.25}(2\theta)$ (l_0=0.012mm)

(g) $b_I=\cos^{0.125}(2\theta)$, $b_{II}=\sin^{0.125}(2\theta)$ (l_0=0.012mm)

(h) b_I=1.0, b_{II}=1.0 (l_0=0.012mm)

Figure 23. Crack paths for the single-inclined notched plate under tension (χ=1.0)

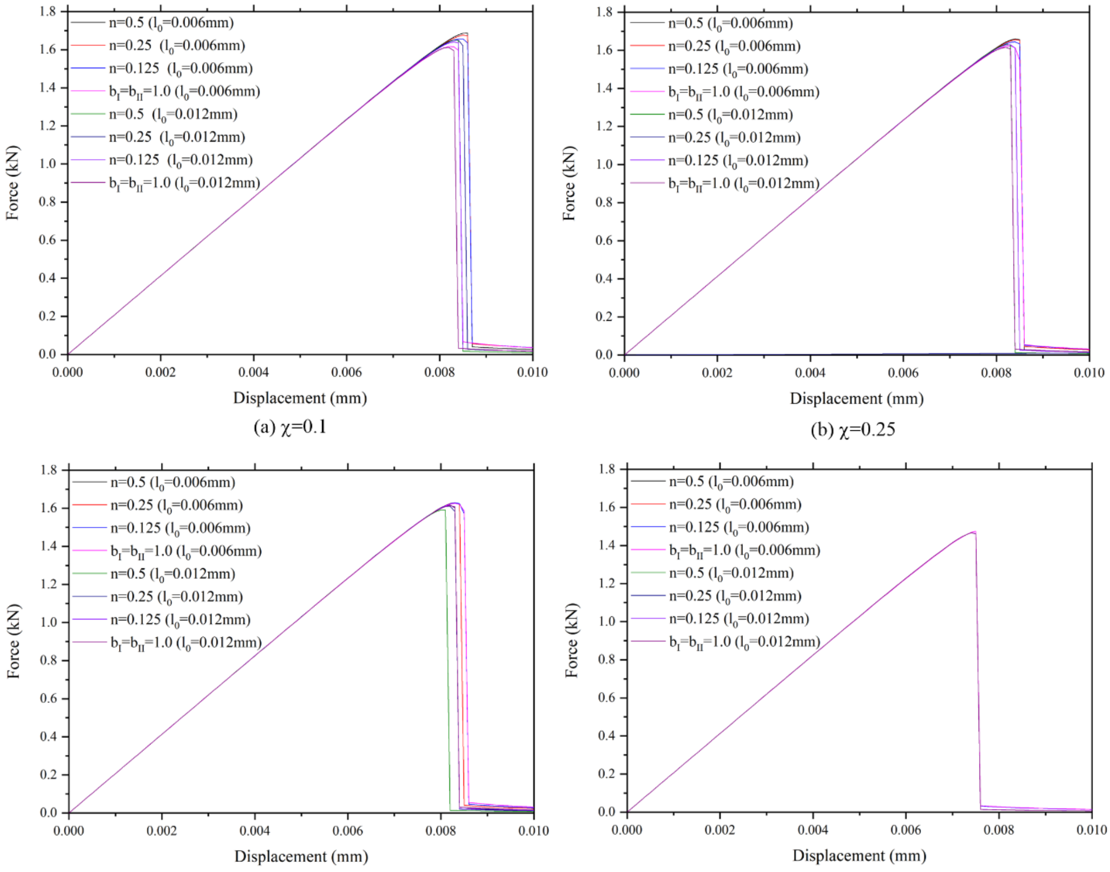

(a) $\chi=0.1$ (b) $\chi=0.25$

(c) $\chi=0.4$ (d) $\chi=1.0$

Figure 24. Load-displacement curves for the single-inclined notched plate under tension

6.4 A rock plate with two inclined notches under uniaxial compression

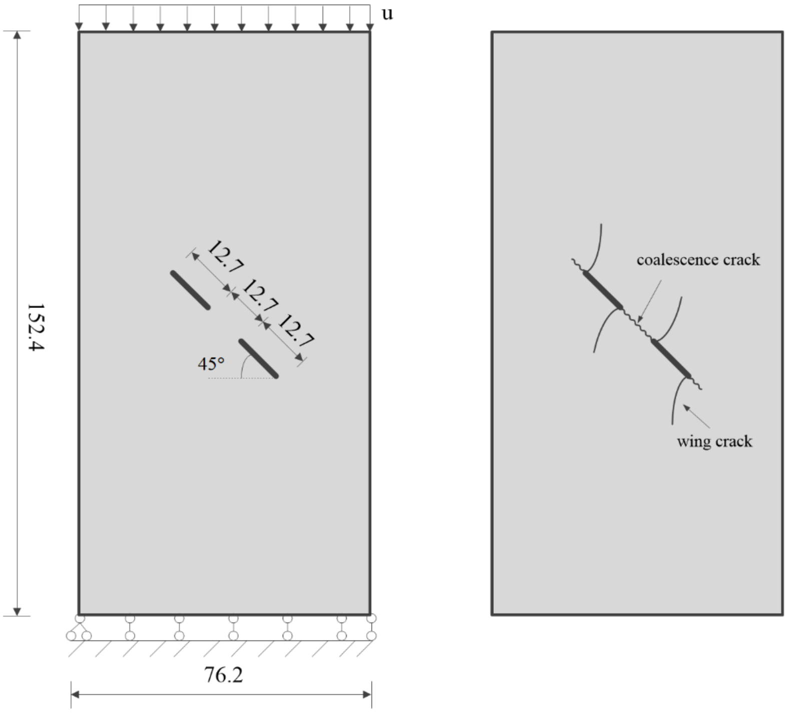

(a) Geometry and boundary conditions (b) Crack paths in experiment

Figure 25. A rock specimen with two notches under uniaxial compression (unit: mm)

To further show the advantage of the proposed model, a rock specimen with two pre-existing notches under uniaxial compression conducted by Bobet et al. [59] is simulated. The geometry and boundary conditions are shown in Figure 25(a). The height and width of the specimen are 152.4mm and 76.2mm respectively, and all the notches have a length of 12.7 mm. The crack paths observed in the experiment are shown in Figure 25(b).

The material properties used in the simulation are Young's modulus $E = 5.96$ GPa, Poisson's ratio $\nu = 0.24$, fracture energy $G_c^t = 50$ N/m, and failure tension strength $f_t = 2.3$ MPa. Four values of χ=0.5, 2.0, 4.0, and 6.0 are considered, and the modified crack direction search algorithm is implemented, especially, $\theta = \pi / 4$ and $\psi_{0II}^{+} = \overline{\tau}^2 / (2\mu)$ are adopted for the case $\overline{\sigma}_1 < 0$, i.e., the material is allowed to damage under compressive-shear stress. The geometric crack function $\alpha(s) = s^2$, degradation function $\omega(s) = (1-s)^2$, and $b_I = b_{II} = 1$ are implemented in this example.

Triangular elements are used to discretize the domain with fine meshes (the mesh size is about 0.1mm) assigned to the critical zones and the length scale is $l_0 = 0.59$ mm. The displacement increment Δu is 10^{-3} mm and the staggered algorithm without iteration [27] between Equations (84) and (85) is applied in this example.

The crack paths obtained by the proposed model are shown in Figure 26, Figure 27, Figure 28, and Figure 29 for different χ. It is indicated that no wing crack is obtained for the case χ=0.5, and shearing cracks are appeared because of the critical shear failure stress is small. On the contrary, four wing cracks are observed for the case χ=6.0, and no shearing crack is obtained, which is because the critical shear failure stress is much greater than the critical normal fracture stress, and the wing cracks emerge because of the tensile stress. For the cases χ=2.0 and 4.0, four wing cracks emerge first, then shearing cracks initiate at the tips of the pre-existing cracks, and finally grow to a coalescence crack between the two pre-existing cracks, which have good agreements with the experiment result shown in Figure 25(b).

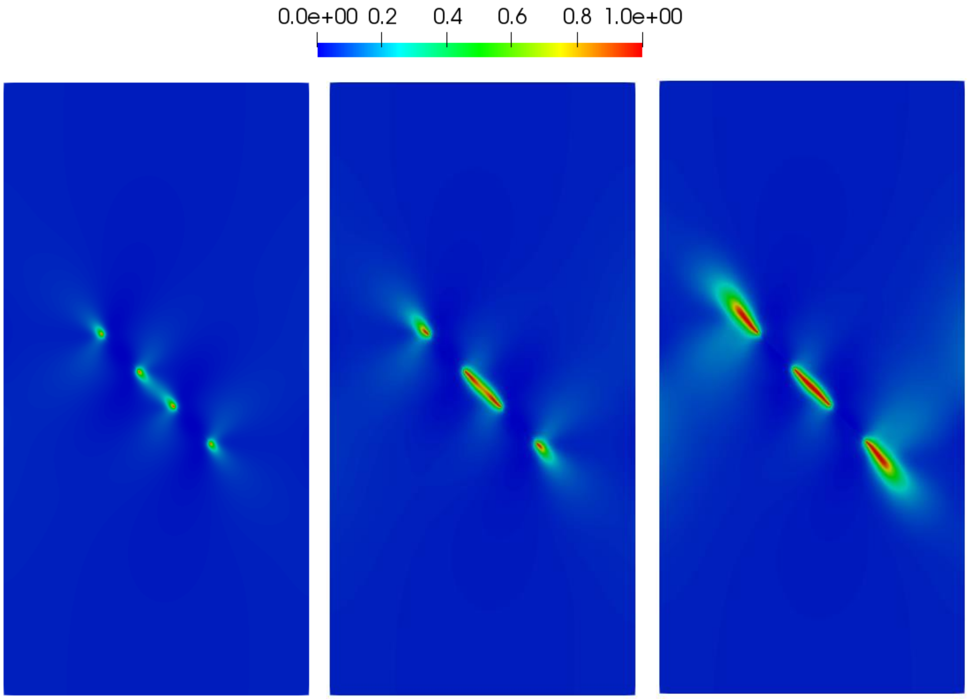

(a) u=0.147 mm (b) u=0.154 mm (c) u=0.160 mm

Figure 26. Crack paths for a rock plate under uniaxial compression (χ =0.5)

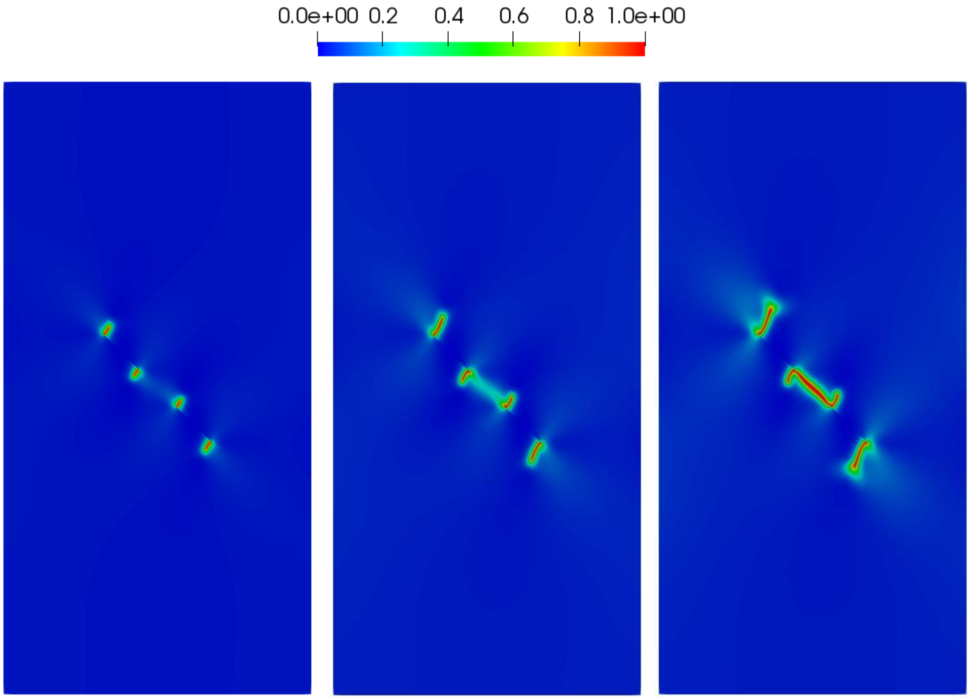

(a) u=0.4 mm (b) u=0.5 mm (c) u=0.511 mm

Figure 27. Crack paths for a rock plate under uniaxial compression (χ =2.0)

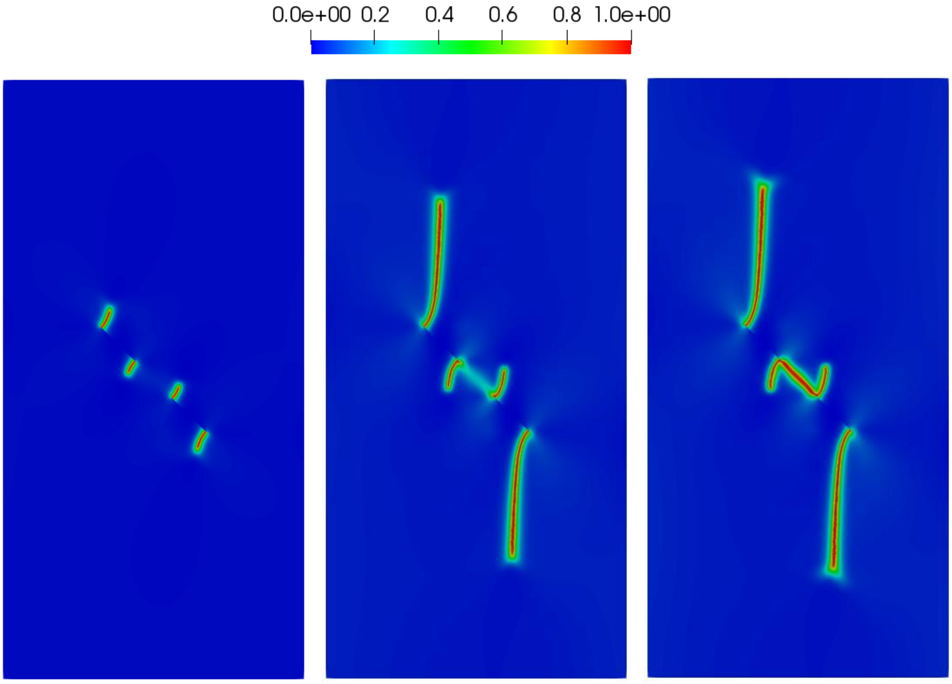

(a) u=0.600 mm (b) u=0.940 mm (c) u=0.950 mm

Figure 28. Crack paths for a rock plate under uniaxial compression (χ =4.0)

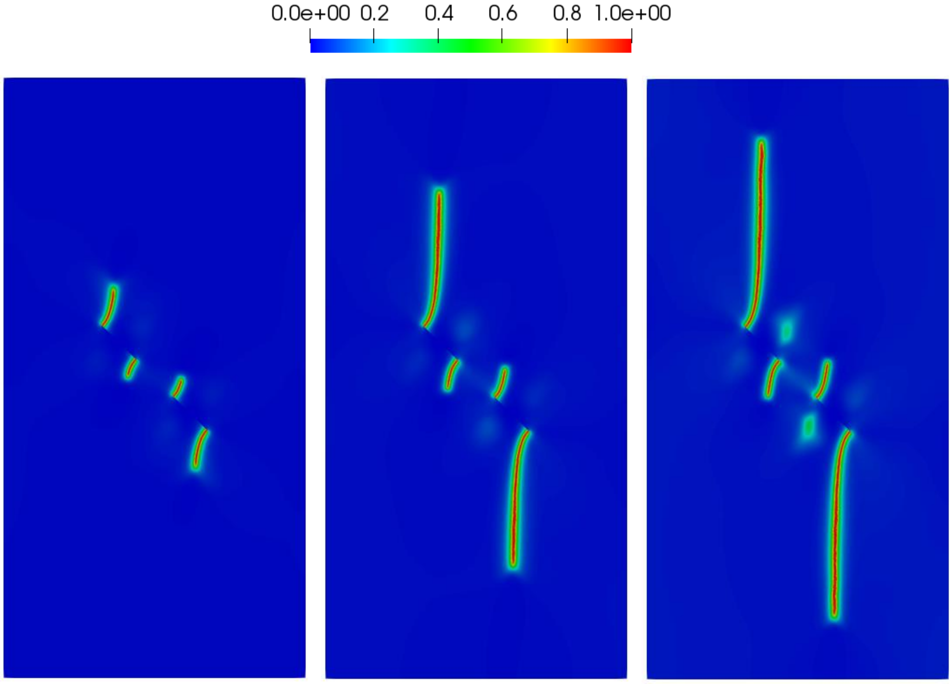

(a) u=0.800 mm (b) u=1.230 mm (c) u=1.235 mm

Figure 29. Crack paths for a rock plate under uniaxial compression (χ =6.0)

7. Conclusions

In this paper, a phase-field model for mixed-mode fracture is proposed. The unified tensile fracture criterion is embedded in the unified phase-field theory. Two additional material parameters are introduced in the proposed model, i.e., the failure tension strength and the ratio of the critical shear failure stress to the critical normal fracture stress. This ratio controls the crack propagation direction. Failure modes based on both maximum normal stress criterion and maximum shear stress criterion are only two special cases in the proposed model.

Several numerical examples have been presented to verify the proposed model. As expected, different failure patterns can be obtained by changing the material property χ (the ratio of the critical shear failure stress to the critical normal fracture stress). For example, a fracture angle close to $\pi/4$ can be obtained if $\chi \to 0$ for a bar under tensile loading. Numerical results have shown that the proposed model can also be applied to rock-like materials under compression.

The influence of different functions of b_I and b_{II} on the crack paths are also investigated in this paper. It has been found that different b_I and b_{II} influence the crack paths in some examples, especially when χ is very small (numerical example 1 and numerical example 3). However, the influence is not very much in most examples and the case $b_I = b_{II} = 1.0$ can also obtain similar results, which can simplify the model since it results in a linear system of equations while solving Equation (84).

Appling the proposed phase-field model to dynamic problems is on-going. Adaptive refinement can be implemented to save computational resources.

Acknowledgments

Financial support for the project from the National Key R&D Program of China (No. 2017YFC0404802) and National Natural Science Foundation of China (No. 51979207, No. 51609181) is acknowledged.

References:

[1] G. Zi and T. Belytschko, *New crack‐tip elements for XFEM and applications to cohesive cracks,* Int. J. Numer. Meth. Eng. 57 (15) (2003) 2221-2240.

[2] S.Z. Feng and X. Han, *A novel multi-grid based reanalysis approach for efficient prediction of fatigue crack propagation,* Comput. Method. Appl. M. 353 (2019) 107-122.

[3] T. Belytschko, L. Gu, and Y. Lu, *Fracture and crack growth by element free Galerkin methods,* Model. Simul. Mater. Sc. 2 (3A) (1994) 519.

[4] H. Ren, X. Zhuang, and T. Rabczuk, *Dual-horizon peridynamics: A stable solution to varying horizons,* Comput. Method. Appl. M. 318 (2017) 762-782.

[5] H. Ren, X. Zhuang, Y. Cai, and T. Rabczuk, *Dual-horizon Peridynamics,* Int. J. Numer. Meth. Eng. 108 (12) (2016) 1451-1476.

[6] T. Rabczuk, G. Zi, S. Bordas, and H. Nguyen-Xuan, *A simple and robust three-dimensional cracking-particle method without enrichment,* Computer Methods in Applied Mechanics & Engineering. 199 (37) (2010) 2437-2455.

[7] T. Rabczuk and T. Belytschko, *Cracking particles: A simplified meshfree method for arbitrary evolving cracks,* Int. J. Numer. Meth. Eng. 61 (13) (2010) 2316-2343.

[8] P. Areias, J. Reinoso, P.P. Camanho, J.C.D. Sá, and T. Rabczuk, *Effective 2D and 3D crack propagation with local mesh refinement and the screened Poisson equation,* Eng. Fract. Mech. 189 (2017) S0013794417307804.

[9] P. Areias, M.A. Msekh, and T. Rabczuk, *Damage and fracture algorithm using the screened Poisson equation and local remeshing,* Eng. Fract. Mech. 158 (2016) 116-143.

[10] F. Yan, P.-Z. Pan, X.-T. Feng, and S.-J. Li, *The continuous-discontinuous cellular automaton method for elastodynamic crack problems,* Eng. Fract. Mech. 204 (2018) 482-496.

[11] F. Yan, P.-Z. Pan, X.-T. Feng, S.-J. Li, and Q. Jiang, *A novel fast overrelaxation updating method for continuous-discontinuous cellular automaton,* Appl. Math. Model. 66 (2019) 156-174.

[12] M. Hofacker and C. Miehe, *Continuum phase field modeling of dynamic fracture: variational principles and staggered FE implementation,* Int. J. Fracture. 178 (1-2) (2012) 113-129.

[13] J.-Y. Wu, V.P. Nguyen, C.T. Nguyen, D. Sutula, S. Bordas, and S. Sinaie, *Phase field modeling of fracture,* Advances in Applied Mechancis: Multi-scale Theory and Computation. 53 (2019).

[14] X. Zhang, C. Vignes, S.W. Sloan, and D. Sheng, *Numerical evaluation of the phase-field model for brittle fracture with emphasis on the length scale,* Comput. Mech. 59 (5) (2017) 737-752.

[15] S. Zhou, X. Zhuang, H. Zhu, and T. Rabczuk, *Phase field modelling of crack propagation, branching and coalescence in rocks,* Theor. Appl. Fract. Mec. 96 (2018) 174-192.

[16] B. Bourdin, G.A. Francfort, and J.-J. Marigo, *Numerical experiments in revisited brittle fracture,* J. Mech. Phys. Solids. 48 (4) (2000) 797-826.

[17] I. Aranson, V. Kalatsky, and V. Vinokur, *Continuum field description of crack propagation,* Phys. Rev. Lett. 85 (1) (2000) 118.

[18] A. Karma, D.A. Kessler, and H. Levine, *Phase-field model of mode III dynamic fracture,* Phys. Rev. Lett. 87 (4) (2001) 045501.

[19] V. Hakim and A. Karma, *Laws of crack motion and phase-field models of fracture,* J. Mech. Phys. Solids. 57 (2) (2009) 342-368.

[20] R. Spatschek, E. Brener, and A. Karma, *Phase field modeling of crack propagation,* Philosophical Magazine. 91 (1) (2011) 75-95.

[21] H. Henry and H. Levine, *Dynamic instabilities of fracture under biaxial strain using a phase field model,* Phys. Rev. Lett. 93 (10) (2004) 105504.

[22] C.-H. Chen, E. Bouchbinder, and A. Karma, *Instability in dynamic fracture and the failure of the classical theory of cracks,* Nature Physics. 13 (12) (2017) 1186.

[23] H. Amor, J.-J. Marigo, and C. Maurini, *Regularized formulation of the variational brittle fracture with unilateral contact: Numerical experiments,* J. Mech. Phys. Solids. 57 (8) (2009) 1209-1229.

[24] C. Kuhn and R. Müller, *A continuum phase field model for fracture,* Eng. Fract. Mech. 77 (18) (2010) 3625-3634.

[25] G.A. Francfort and J.-J. Marigo, *Revisiting brittle fracture as an energy minimization problem,* J. Mech. Phys. Solids. 46 (8) (1998) 1319-1342.

[26] J.-Y. Wu, *A unified phase-field theory for the mechanics of damage and quasi-brittle failure,* J. Mech. Phys. Solids. 103 (2017) 72-99.

[27] C. Miehe, M. Hofacker, and F. Welschinger, *A phase field model for rate-independent crack propagation: Robust algorithmic implementation based on operator splits,* Comput. Method. Appl. M. 199 (45) (2010) 2765-2778.

[28] G. Lancioni and G. Royer-Carfagni, *The variational approach to fracture mechanics. A practical application to the French Panthéon in Paris,* J. Elasticity. 95 (1-2) (2009) 1-30.

[29] J.-Y. Wu and M. Cervera, *A novel positive/negative projection in energy norm for the damage modeling of quasi-brittle solids,* Int. J. Solids. Struct. 139-140 (2018) 250-269.

[30] C. Steinke and M. Kaliske, *A phase-field crack model based on directional stress decomposition,* Comput. Mech. 63 (5) (2019) 1019-1046.

[31] J.-Y. Wu, V.P. Nguyen, H. Zhou, and Y. Huang, *A variationally consistent phase-field anisotropic damage model for fracture,* Comput. Method. Appl. M. 358 (2020) 112629.

[32] C.J. Larsen, C. Ortner, and E. Süli, *Existence of solutions to a regularized model of dynamic fracture,* Mathematical Models and Methods in Applied Sciences. 20 (07) (2010) 1021-1048.

[33] B. Bourdin, C.J. Larsen, and C.L. Richardson, *A time-discrete model for dynamic fracture based on crack regularization,* Int. J. Fracture. 168 (2) (2011) 133-143.

[34] M.J. Borden, C.V. Verhoosel, M.A. Scott, T.J. Hughes, and C.M. Landis, *A phase-field description of dynamic brittle fracture,* Comput. Method. Appl. M. 217 (2012) 77-95.

[35] M. Hofacker and C. Miehe, *A phase field model of dynamic fracture: Robust field updates for the analysis of complex crack patterns,* Int. J. Numer. Meth. Eng. 93 (3) (2013) 276-301.

[36] A. Schlüter, A. Willenbücher, C. Kuhn, and R. Müller, *Phase field approximation of dynamic brittle fracture,* Comput. Mech. 54 (5) (2014) 1141-1161.

[37] H.L. Ren, X.Y. Zhuang, C. Anitescu, and T. Rabczuk, *An explicit phase field method for brittle dynamic fracture,* Comput. Struct. 217 (2019) 45-56.

[38] F. Amiri, D. Millán, Y. Shen, T. Rabczuk, and M. Arroyo, *Phase-field modeling of fracture in linear thin shells,* Theor. Appl. Fract. Mec. 69 (2014) 102-109.

[39] P. Areias, T. Rabczuk, and M.A. Msekh, *Phase-field analysis of finite-strain plates and shells including element subdivision,* Comput. Method. Appl. M. 312 (2016) 322-350.

[40] M.A. Msekh, N.H. Cuong, G. Zi, P. Areias, X. Zhuang, and T. Rabczuk, *Fracture properties prediction of clay/epoxy nanocomposites with interphase zones using a phase field model,* Eng. Fract. Mech. 188 (2018) 287-299.

[41] C.V. Verhoosel and R. de Borst, *A phase ‐field model for cohesive fracture,* Int. J. Numer. Meth. Eng. 96 (1) (2013) 43-62.

[42] J. Vignollet, S. May, R. De Borst, and C.V. Verhoosel, *Phase-field models for brittle and cohesive fracture,* Meccanica. 49 (11) (2014) 2587-2601.

[43] S. May, J. Vignollet, and R. De Borst, *A numerical assessment of phase-field models for brittle and cohesive fracture: Γ-convergence and stress oscillations,* European Journal of Mechanics-A/Solids. 52 (2015) 72-84.

[44] S. Conti, M. Focardi, and F. Iurlano. *Phase field approximation of cohesive fracture models*. in *Annales de l'Institut Henri Poincare (C) Non Linear Analysis*. 2016. Elsevier.

[45] R. Alessi, J.-J. Marigo, C. Maurini, and S. Vidoli, *Coupling damage and plasticity for a phase-field regularisation of brittle, cohesive and ductile fracture: one-dimensional examples,* Int. J. Mech. Sci. 149 (2018) 559-576.

[46] V.P. Nguyen and J.-Y. Wu, *Modeling dynamic fracture of solids with a phase-field regularized cohesive zone model,* Comput. Method. Appl. M. 340 (2018) 1000-1022.

[47] D. Chu, X. Li, Z. Liu, J. Cheng, T. Wang, Z. Li, and Z. Zhuang, *A unified phase field damage model for modeling the brittle-ductile dynamic failure mode transition in metals,* Eng. Fract. Mech. 212 (2019) 197-209.

[48] Z. Zhang and J. Eckert, *Unified tensile fracture criterion,* Phys. Rev. Lett. 94 (9) (2005) 094301.

[49] X. Zhang, S.W. Sloan, C. Vignes, and D. Sheng, *A modification of the phase-field model for mixed mode crack propagation in rock-like materials,* Comput. Method. Appl. M. 322 (2017) 123-136.

[50] B. Shen and O. Stephansson, *Modification of the G-criterion for crack propagation subjected to compression,* Eng. Fract. Mech. 47 (2) (1994) 177-189.

[51] E.C. Bryant and W. Sun, *A mixed-mode phase field fracture model in anisotropic rocks with consistent kinematics,* Comput. Method. Appl. M. 342 (2018) 561-584.

[52] J.-Y. Wu and V.P. Nguyen, *A length scale insensitive phase-field damage model for brittle fracture,* J. Mech. Phys. Solids. 119 (2018) 20-42.

[53] B. Bourdin, G.A. Francfort, and J.-J. Marigo, *The variational approach to fracture,* J. Elasticity. 91 (1-3) (2008) 5-148.

[54] C. Miehe, F. Welschinger, and M. Hofacker, *Thermodynamically consistent phase‐field models of fracture: Variational principles and multi‐field FE implementations,* Int. J. Numer. Meth. Eng. 83 (10) (2010) 1273-1311.

[55] J.-Y. Wu and M. Cervera, *On the equivalence between traction- and stress-based approaches for the modeling of localized failure in solids,* J. Mech. Phys. Solids. 82 (2015) 137-163.

[56] M. Cervera and J.-Y. Wu, *On the conformity of strong, regularized, embedded and smeared discontinuity approaches for the modeling of localized failure in solids,* Int. J. Solids. Struct. 71 (2015) 19-38.

[57] J.-Y. Wu and M. Cervera, *A thermodynamically consistent plastic-damage framework for localized failure in quasi-brittle solids: Material model and strain localization analysis,* Int. J. Solids. Struct. 88-89 (2016) 227-247.

[58] M. Ambati, T. Gerasimov, and L. De Lorenzis, *A review on phase-field models of brittle fracture and a new fast hybrid formulation,* Comput. Mech. 55 (2) (2015) 383-405.

[59] A. Bobet and H.H. Einstein, *Numerical modeling of fracture coalescence in a model rock material,* Int. J. Fracture. 92 (3) (1998) 221.